Unravelling the Dust-Gas Dynamics in the Rings of Protoplanetary Disks

Maya Tatarelli

Supervised by Prof. Eve J. Lee

Department of Physics

McGill University

Montréal, Québec, Canada

August 15, 2024

A thesis presented for the degree of Masters of Science

Abstract

Radio interferometric images have revealed that concentric dust rings are a common feature of protoplanetary disks. These rings provide observational evidence that there are mechanisms to slow and even halt the expected rapid inward radial drift of dust particles. As they are areas of high density, they are also thought to be potential sites for planetesimal, and eventually planet, formation. How efficiently the dust grains collect into these rings is dependent on the source of pressure perturbations in the disk gas and the size of the grains themselves. We investigate this dust trapping efficiency and the dust-gas dynamics within the pressure bump using GIZMO, a particle-based hydrodynamics code, by performing 2D global disk and 3D local shearing box simulations of protoplanetary disks with an embedded planet to establish the pressure bump. Using the dust-to-gas mass ratio and turbulent viscosity within the pressure bump, we will provide some initial calculations on the coagulation and formation of dust clumps within the rings. Our 3D local shearing box simulation is run with a planet of mass $M_p = 0.5 M_{\rm th}$ and particle Stokes number $\tau_S = 0.1$. From our preliminary 3D results, we find that within the pressure bump

and the particle disk scale height, the dust-to-gas mass ratio is above the critical ratio required for dust clumping by the streaming instability. The 2D global disk simulation is still in development, so we present the progress thus far and discuss the current code behaviour and future modifications required.

Abrégé

Les images radio-interférométriques ont révélé que les anneaux concentriques de poussière sont une caractéristique commune aux disques protoplanétaires. Ces anneaux prouvent qu'il existe des mécanismes permettant de ralentir, et même d'arrêter, la dérive radiale et rapide des particules de poussière, vers l'intérieur du disque. Etant donné que ces anneaux sont des zones de densité élevée, on pense qu'ils sont également des sites potentiels pour la formation de planétésimaux et, finalement, de planètes. L'efficacité de l'accumulation de poussière dans ces anneaux dépend de la source des perturbations de pression dans le gaz et de la taille des particules elles-mêmes. Nous utilisons le code hydrodynamique basé sur les particules GIZMO pour étudier l'efficacité des pièges à poussière et la dynamique gaz-poussière au sein du maximum de pression dans les disques protoplanétaires. Cela implique des simulations globales en 2D ainsi que des simulations locales en 3D de boîtes de cisaillement avec une planète intégrée pour déterminer les conditions du maximum de pression. En utilisant le rapport de masse poussière/gaz et la viscosité turbulente dans le maximum de pression, nous fournirons des calculs initiaux sur la coagulation et la formation d'amas de poussière

dans les anneaux. Notre simulation 3D de boîte de cisaillement locale est effectuée avec une planète de masse $M_p = 0.5 M_{\rm th}$ et un nombre de Stokes des particules $\tau_S = 0.1$. D'après nos résultats préliminaires en 3D, nous constatons qu'à l'intérieur de la perturbation de pression et de la hauteur caractéristique du disque de particules, le rapport de masse poussière/gaz est supérieur au rapport critique requis pour l'agglomération de la poussière par l'instabilité de courant. La simulation globale du disque en 2D est encore en cours de développement. Nous présentons donc les progrès réalisés jusqu'à présent et discutons des performances actuelles du code ainsi que des modifications futures requises.

Acknowledgements

First and foremost, I want to express my deepest gratitude to my supervisor, Prof. Eve Lee. Your support began even before I started my master's degree and has never wavered. Our discussions about physics, fluids, and the frustrating boundary conditions have been incredibly valuable. You've taught me so much and helped shape me into a more confident and capable researcher. I will carry this with me into all my future endeavours. I also want to extend my heartfelt thanks to Prof. Siva Nadarajah and Prof. Andrew Cumming for their guidance and support. Your contributions have been crucial to advancing my research and academic growth.

To my parents, thank you for creating an environment that fosters curiosity and learning. Your support has been more than I could have ever asked for. Thanks to my dad for his enthusiasm about everything I was learning and for always being excited to hear about my physics discoveries. And a big thank you to my mom for her calming presence during my most stressful times and, of course, for making me coffee and helping me write my emails. To my sister Emma, thank you for encouraging me and helping me unwind when I needed

a break. And to my closest friend throughout this journey, Rawan, who turned even the toughest moments into some of my best memories and always pushed me to be better. I also want to remember my grandfather, whom I lost just as I was beginning my studies at McGill, as well as my grandmothers, who were my biggest cheerleaders and whom I lost during my master's. I wish more than anything that I could share this moment with them.

And last but certainly not least, to my research group and friends—Amy Karalis, Kevin Marimbu, Vincent Savignac, Tim Hallat, and Emilia Vlahos—thank you for being there every step of the way, sharing in our struggles, and making our conference journey to Exoplanets5 unforgettable. A special shout-out to Amy for always looking out for us and for her uncanny ability for finding free food, and to Emilia who could always make me laugh when I needed it most. You all made my time at McGill something I'll never forget and will always look back on fondly.

Contents

List of Figures

List of Tables

List of Acronyms

ALMA	Atacama Large Millimeter/submillimeter Array.
DSHARP	Disk Substructures at High Angular Resolution Project.
GI	Gravitational Instability.
MFM	Meshless Finite Mass.
RMS	Root Mean Squared.
SI	Streaming Instability.
SPH	Smoothed Particle Hydrodynamics.

Chapter 1

Introduction

Observations of protoplanetary disks have revealed that dust and gas substructures are ubiquitous among the observed disks (see, e.g., Andrews et al., 2018). However, due to the relative velocity between the dust and the sub-Keplerian gas, we expect rapid inward radial drift of the dust grains, suggesting that they drift onto the star on timescales several orders of magnitude shorter than the typical disk lifetime of ∼few Myr (Mamajek, 2009). The growth from sub-micron sized dust particles into larger objects thus presents many physical challenges. These substructures therefore provide observational evidence which suggests there is some mechanism slowing, and even halting, the rapid inward drift. Such a mechanism may be a pressure bump in the disk gas. A pressure perturbation in a disk with an otherwise monotonically decreasing radial gas pressure profile can act as a dust trap, halting the inward drift and allowing the survival and collection of dust grains in the disk

on timescales appropriate for planetesimal formation.

As these observations make it evident that dust can be trapped within pressure bumps, our goal is to investigate the dust-gas dynamics within these pressure bumps to determine whether they are capable of dust coagulation, clumping, and eventually forming cores capable of growth by pebble accretion. We perform both 2D global disk and 3D local shearing box simulations, using the particle-based hydrodynamic code, GIZMO. We choose GIZMO over other hydrodynamic codes because it is the only publicly available code that supports self-gravity, and does so not only for dust particles, but also gas. Although self-gravity is not necessary for initial dust clumping to occur, it is required to keep the clump intact against tidal shearing over time.

Our objective is to develop the GIZMO code and the 2D/3D simulation setups and initial conditions, so that they behave physically over the relevant timescales, while also reducing the error associated with numerical artifacts from the code's hydrodynamic solvers. In particular, our goal is to ensure that the boundary conditions in both the global and local shearing box simulations do not introduce error that is then propagated through the simulation domain, affecting the dynamics of the dust and gas behaviour, so we aim to achieve a specified target precision of the relevant disk properties.

Chapter 2

Literature Review

Over the past two decades, the exoplanet community has successfully detected over 5000 exoplanets (NASA Exoplanet Archive, 2024). It is confirmed that planet formation is not an event isolated to our solar system, which begs the question, how are planets and planetary systems born? Thoroughly answering this question requires an understanding of the entire planet formation process, all the way back to the birth of the young host star and its circumstellar disk of dust and gas, known as a protoplanetary disk.

Early on in this process, the growth from sub-micron sized dust particles into larger objects involves complex processes which present many physical challenges (Pinilla et al., 2012). In a smooth disk with a radial gas pressure that monotonically decreases with radius, the gas moves at a sub-Keplerian velocity due to the outwards gas pressure gradient force. The dust particles, which do not experience this pressure gradient force and orbit at Keplerian

velocities, feel a headwind from the gas, which causes the dust to lose angular momentum and drift inwards. Typically, we invoke mm to cm-sized dust grains at the midplane in the outer disk regions (> 50 AU) to match mm to cm-wave spectra and images (e.g., D'Alessio et al., 2001; Testi et al., 2003), assuming an optically thin disk. Around ~ 50 AU, these grains have characteristic lifetimes (due to radial drift towards the star) between 10^5 yr down to 10^3 yr (Weidenschilling, 1977), approximately $1-3$ orders of magnitude shorter than the typical disk characteristic lifetime of ~ 2.5 Myr (Mamajek, 2009). As a result, the dust moves toward the star before a large object can be formed. Furthermore, the solid particles can reach velocities that lead to fragmentation by collisions, further preventing dust particles from forming larger bodies. This problem is commonly referred to as the "meter-size barrier", as a one-meter-sized object at 1 AU moves towards the star on timescales as short as 100 years, 4 orders of magnitude shorter than the ∼few Myr disk lifetime, preventing the growth of any larger objects.

However, protoplanetary disk surveys reveal that the dust remains in the outer regions of disks over Myr timescales, providing observational evidence that there must be some mechanism slowing and even preventing the rapid inward radial drift of the dust. One survey in particular is the Disk Substructures at High Angular Resolution Project (DSHARP), conducted using the Atacama Large Millimeter/submillimeter Array (ALMA) (Andrews et al., 2018). This survey found that dust substructures are ubiquitous in the 20 nearby, bright disks that were imaged, most commonly manifesting as rings and gaps, but also as

spirals and crescents (Andrews et al., 2018), shown in Figure 2.1. As such, these substructures may be the key to explaining the mechanism responsible for preventing the radial drift of the dust. Furthermore, as these substructures are areas of high density, they may be appropriate sites for planet formation, thus playing a crucial role in the overall formation process. However, Lee (2024) suggests that this may not be the case in the outer disk regions, so further discussion on this topic is required before any concrete conclusions can be made.

As observations indicate that dust grains persist over $\sim$ few Myr timescale, the mechanism acting to prevent the rapid inward radial drift may help us to understand how grain growth in disks can overcome the meter-size barrier. Unfortunately, the inner disk region is challenging to observe, as its small size on the sky makes it difficult to spatially resolve, and it is optically thick. The outer disk region (> 50AU), on the other hand, is more accessible for observations because it is much easier to spatially resolve and we assume the dust thermal emission to be optically thin at millimeter wavelengths. In addition, in the outer regions of the disk, the meter-size barrier is equivalent to a "millimetre-size barrier", and millimetre observations of the outer region probe precisely this grain size range (Pinilla et al., 2012). So, probing the outer disk region and studying the dust growth may provide insight into the planet formation processes in the inner regions.

The question is then, what mechanism acts to trap the dust and prevent the rapid inward drift? In the presence of a gas pressure perturbation in the disk, the relative velocities of the dust and gas due to the gas pressure gradients on either side of the pressure peak cause

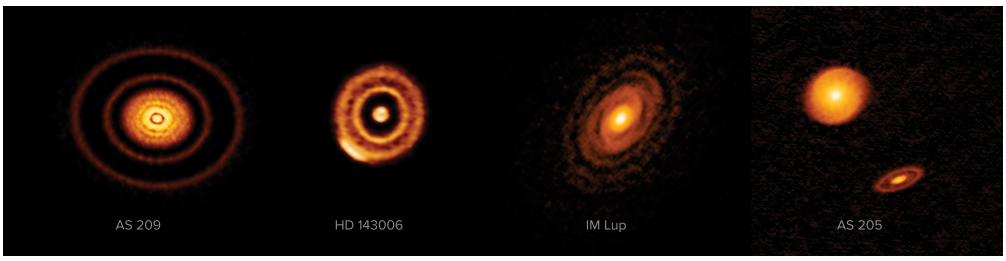

Figure 2.1: Imaged protoplanetary disks showing substructures in the form of rings, gaps, and spirals. Credit: ALMA (ESO/NAOJ/NRAO), S. Andrews et al.; NRAO/AUI/NSF, S. Dagnello.

the dust to drift towards the peak, trapping it within the bump. We therefore must consider a disk with a radial gas pressure profile that is not monotonically decreasing with radius. Although a variety of possible sources of gas perturbations have been suggested to explain the formation of pressure bumps in the disk, one plausible and widely postulated hypothesis are gaps carved by perturbations from massive planets embedded in the disk, which is what we will focus on.

The literature review will proceed as follows: Section 2.1 will discuss the dust-gas dynamics within the disk, including dust-coupling to the gas and radial drift; Section 2.2 will describe the formation mechanism of the gas pressure bump due to an embedded planet in the disk; Section 2.3 will discuss the mechanism by which this pressure bump collects and traps the dust within it; Section 2.4 will further discuss the dust-gas dynamics within the pressure bump, including the processes responsible for dust coagulation, clumping, and core growth; and, finally, Section 2.5 will present recent studies which also apply hydrodynamic codes to investigate dust-gas dynamics and planetesimal formation in

protoplanetary disks.

2.1 Dust-Gas Dynamics in Disks

When dust particles move through a gas with some relative velocity, the dust experiences a drag force. The type of drag force acting on the dust may be either Stokes drag or Epstein drag, for $a \gg \lambda_{\rm mfp}$ or $a \lesssim \lambda_{\rm mfp}$, respectively, where a is the size of the dust grain and $\lambda_{\rm mfp} = 1/{\rm n}\sigma$ is the mean free path (mfp) of the gas (i.e., the average distance a gas particle will travel before colliding with another particle). The mfp is written in terms of σ, the collisional cross-sectional area of the gas particles, and ${\rm n} = \rho/\mu m_{\rm H}$, the volume number density, where ρ is the volume mass density, μ is the mean molecular weight, and $m_{\rm H}$ is the mass of a hydrogen atom.

In our simulations, we are primarily interested in dust grains which are smaller than or comparable in size to the gas mean free path, so we assume an Epstein drag law. In the presence of a drag force, we define the dust particle stopping time as the time it takes a particle with a given momentum to reach its terminal velocity, i.e., the velocity at which the net force is zero (Pinilla et al., 2012). It is given by

$$t_{\rm s} = \frac{\rho_a a}{\rho_g c_s}, \tag{2.1}$$

where ρ_a is the material density of a dust grain, ρ_g is the volumetric mass density of the disk

gas, and $c_s = \sqrt{\frac{k_B T}{\mu m_{\rm H}}}$ is the gas sound speed (with the Boltzmann constant k_B). We can then characterize the dust particles using a dimensionless stopping time parameter, known as the particle Stokes number

$$\tau_S = t_s \Omega_K = \Omega_K \frac{\rho_a a}{\rho_g c_s}, \tag{2.2}$$

i.e., the momentum-stopping time normalized to the local orbital time. The Keplerian orbital frequency is given by $\Omega_K = \sqrt{GM_*/r^3}$, where G is the gravitational constant and r is the orbital distance from the star.

As previously explained, the dust grains drift radially inwards through the disk as they lose angular momentum. The drift velocity is given by Weidenschilling (1977)

$$\dot{r} = -2\eta v_K \frac{\tau_S}{1+\tau_S^2}, \tag{2.3}$$

where $v_K = \Omega_K r$ is the Keplerian orbital velocity of the dust grain, $\eta \equiv -\frac{1}{2}\left(\frac{H}{r}\right)^2 \frac{\partial \ln \mathrm{P}}{\partial \ln r}$, $H = \frac{c_s}{\Omega_K}$ is the disk gas scale height, and $\frac{\partial \ln \mathrm{P}}{\partial \ln r} = \beta$ is the pressure gradient term which follows a power law according to $\mathrm{P} \propto r^\beta$. The power law index β is determined by the density and temperature profiles of the gas in the disk through the equation of state for pressure $P = \rho c_s^2 \propto \rho T \propto r^{-p} r^{-q} \propto r^{-(p+q)}$, so that $\beta = -(p+q)$.

We see that when $\tau_S \ll 1$, $\dot{r} \to 0$, because the particles are well coupled to the gas and flow with it. When $\tau_S \gg 1$, $\dot{r} \to 0$, because the large particles do not care about the gas flow and continue to flow in their regular orbit. The radial drift is maximized when $\tau_S \sim 1$. This

is relevant for our understanding of the dust-gas dynamics within the gas pressure bump in the disk, which will be discussed further in Section 2.3 and 2.4.

2.2 Gas Pressure Bump Formation in Disks

This section will present the the formation process of a pressure bump in the disk gas due to an embedded planet. A relevant length scale to consider is the Hill radius, given by

$$R_{\text{Hill}} = r\left(\frac{M_p}{3M_*}\right)^{1/3}, \tag{2.4}$$

where M_p is the planet mass and M_* is mass of the central star. The Hill radius is the spatial extent of the embedded planet's gravitational influence against the tidal acceleration from the star the planet orbits. When the Hill radius is comparable to the disk scale height H, this yields what is known as the "thermal mass"

$$M_{\text{th}} = \frac{2c_s^3}{3G\Omega_K}. \tag{2.5}$$

The presence of an embedded planet in the gas disk can excite density waves (Dong et al., 2017) which carry both energy and angular momentum, and when a wave is dissipated, angular momentum is deposited in the disk gas (Lin & Papaloizou, 1993). In an inviscid or low viscosity disk, the waves dampen less by viscous dissipation, and more by steepening and

then breaking. It is at this breaking point that the wave deposits its angular momentum. The result is that the gas is repelled away from the planet, carving out the gaps in the vicinity of the planet's orbit. From Goodman & Rafikov (2001), they show that the waves launched to either side of the planet's orbit will travel a radial distance

$$l_{\rm sh} \approx 0.8 \left(\frac{\gamma + 1}{12/5} \frac{M_p}{M_{\rm th}} \right)^{-2/5} H, \tag{2.6}$$

where γ is the adiabatic index, before shocking and dissipating. The gas originally in the gap regions is pushed away and piled up at the gap edges to form regions of high gas pressure, and hence the gas pressure bump.

2.3 Gas Pressure Bump as a Dust Trap

The question is then how do the dust particles collect in a gas pressure bump? Let us consider a local radial pressure maximum in the disk at radius $r_{\rm max}$, as shown in Figure 2.2. At $r < r_{\rm max}$ (left of pressure max), gas is super-Keplerian due to the adverse pressure gradient force directed inwards. At $r > r_{\rm max}$ (right of pressure max), the gas is sub-Keplerian due to the additional pressure gradient force directed outwards. Therefore, dust particles receive a tailwind at $r < r_{\rm max}$, and feel a headwind at $r > r_{\rm max}$. The tailwind gives the dust particles angular momentum, drifting them radially outwards (towards pressure peak), while the headwind removes angular momentum causing inward radial drift (also towards

the pressure peak, but from the other side). Overall, the dust migrates towards the pressure maximum from both sides. The dust also exerts a drag force on the gas, known as dust 'back-reaction', which drags more gas into the perturbation and acts to further grow the pressure bump.

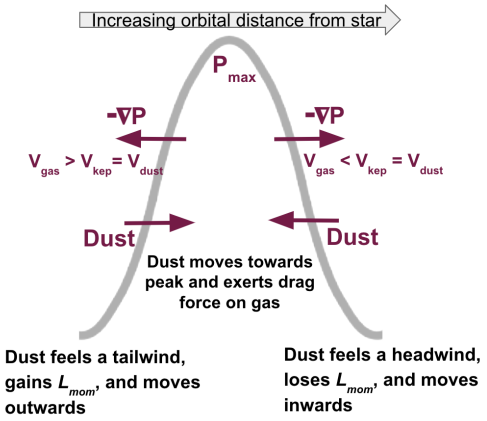

Figure 2.2: Schematic of the streaming instability acting on dust due to a gas pressure perturbation. A runaway process leads to the collection of dust within the pressure maxima which acts as a dust trap, eventually forming substructures within the disk.

2.4 Dust Coagulation and Clumping

We are also interested in investigating the ability of these dust rings to form planetesimals and eventually planets. Even if pressure perturbations in the disk act as efficient dust traps, we also require some mechanism to coagulate the dust and begin the early stages of planet formation. In this section, we will review the current understanding of the necessary conditions and criteria which must be met for coagulation, clumping, and eventually core

growth to occur.

2.4.1 Streaming Instability

The streaming instability (SI) (Youdin & Goodman, 2005) arises from the mutual interactions of gas and dust via aerodynamic drag. The SI involves a minimal amount of physics, namely, Keplerian orbital motion, gas pressure, and a drag acceleration that is linear in relative velocities. It will always be active in the linear instability regime as long as there is some relative velocity between the dust and gas. The differential motion can concentrate dust particles into streams, forming regions of enhanced dust density. Unlike the gravitational instability (GI), SI does not require self-gravity, yet it generates growing particle-density perturbations that could potentially seed planetesimal formation. In a gas pressure bump, SI is not active at the pressure maximum because there is zero pressure gradient, so both the gas and dust move at Keplerian velocities. Rather, SI will be active on either side of the peak where there exists a non-zero drift velocity of grains.

Although SI is always active in the linear regime as long as there is some relative velocity, it is also possible for the SI to produce strong particle clumping if it is active in the nonlinear instability regime. For SI clumping, the ratio of the average solid to gas surface density, or metallicity, ($Z = \langle \Sigma_d / \Sigma_g \rangle$, where Σ_d and Σ_g are the dust and gas surface densities, respectively) must exceed a critical value (Li & Youdin, 2021). This exact value is set by τ_S and the level of turbulence (characterized by the turbulent viscosity parameter α

(Shakura & Sunyaev, 1973)). Li & Youdin (2021) quantify the thresholds by performing a suite of vertically stratified SI simulations over a range of dust sizes, dust-to-gas ratios, and turbulence levels.

In the disk, particle settling competes with stirring by the gas to establish the particle scale height $H_{\rm p} = \sqrt{H_{{\rm p},\eta}^2 + H_{{\rm p},\alpha}^2}$, where $H_{{\rm p},\eta} \equiv h_\eta \eta r$ is the particle scale height without additional turbulence beyond the dust–gas interactions that drive the SI, and is measured in the SI simulations performed by Li & Youdin (2021), written as a fraction h_η of the SI length scale ηr (Youdin & Goodman, 2005), and $H_{{\rm p},\alpha}/H = \sqrt{\alpha/(\alpha+\tau_S)}$ for additional turbulence which increases stirring (Youdin & Lithwick, 2007). The particle settling and stirring also establishes the dust-to-gas density ratio at the disk midplane, written as

$$\epsilon_\alpha = \frac{\Sigma_d}{\Sigma_g}\frac{H}{H_{\rm p}} = \frac{Z}{\sqrt{h_\eta^2 \Pi^2 + \frac{\alpha}{\alpha+\tau_S}}}, \tag{2.7}$$

where $\Pi = \eta v_K / c_s$ is the parameterized global radial pressure gradient, known as the headwind parameter. Additional turbulence can provide additional stirring, thus increasing $H_{\rm p}$ and reducing the midplane particle density. Therefore, a critical value for the density at the midplane must also be considered for SI clumping in the presence of additional turbulence, given by the following piecewise quadratic function fitting $\log(\epsilon_{\rm crit})$ as a function of $\log(\tau_S)$ to the simulation results of Li & Youdin (2021):

$$\log(\epsilon_{\rm crit}) \approx A(\log\tau_S)^2 + B(\log\tau_S) + C, \tag{2.8}$$

with

$$\begin{cases} A = 0, B = 0, C = \log(2.5) & \text{if } \tau_s < 0.015 \\ A = 0.48, B = 0.87, C = -0.11 & \text{if } \tau_s > 0.015. \end{cases}$$

They present a single criterion for SI clumping including additional turbulence, which can be expressed as a condition on the particle metallicity Z as

$$Z > Z_{\text{crit},\alpha} \equiv \epsilon_{\text{crit}}(\tau_S)\sqrt{h_\eta^2 \Pi^2 + \frac{\alpha}{\alpha + \tau_S}} \approx \epsilon_{\text{crit}}(\tau_S)\sqrt{\left(\frac{\Pi}{5}\right)^2 + \frac{\alpha}{\alpha + \tau_S}}, \tag{2.9}$$

where they find a characteristic $h_\eta \approx 0.2$, with variations about that value that have a complicated τ_S and Z dependence, but stating this to be sufficiently accurate considering uncertainties in simulations and real disks. To apply this criterion, the local disk values of Z, Π, α, and τ_S must be considered, and ϵ_{crit} is calculated using Equation 2.8.

A key result is that in a smooth disk, strong particle clumping occurs at subsolar metallicities ($Z_{\text{crit}} < 0.01$) for $\tau_S > 0.01$, with the lowest $Z_{\text{crit}} = 0.004$ for dust grains with $\tau_s = 0.3$. Smaller particles ($\tau_S < 0.01$), however, require a supersolar threshold ($Z_{\text{crit}} > 0.02$). When the authors include the effects of additional non-SI turbulence, they find that the required midplane dust-to-gas ratios are $\epsilon_{\text{crit}} \lesssim 0.5$ for $0.02 < \tau_S < 1$, and $\epsilon_{\text{crit}} \sim 2.5$ for $\tau_S \leq 0.01$.

2.4.2 Dust Clumping

In the previous section, we discuss the possibility of dust clumping due to the streaming instability, but what are the conditions required for a dust clump to be bound? In order to be considered bound, the clump must be stable against both turbulent diffusion and tidal shear. For the first of these criteria, let us consider the contraction timescale

$$t_{\rm contr} = \frac{\Omega_K}{4\pi G \rho_{\rm cl} \tau_S} \tag{2.10}$$

where $\rho_{\rm cl} = 3M_{\rm cl}/4\pi R_{\rm cl}^3$ is the density of the clump ($M_{\rm cl}$ and $R_{\rm cl}$ are the mass and radius of the clump, respectively), and the diffusion timescale

$$t_{\rm diff} = \frac{R_{\rm cl}^2}{D_d} = \frac{R_{\rm cl}^2 \Omega_K}{v_{\rm rms,cl}^2 \tau_S}, \tag{2.11}$$

where $D_d = v_{\rm rms,cl}^2 \tau_S / \Omega_K$ is the particle diffusion coefficient, and $v_{\rm rms,cl}$ is the root mean squared dispersion velocity of the dust particles in the clump. To be stable against turbulent diffusion, Klahr et al. (2018) and Gerbig et al. (2020) outline the diffusion-limited collapse criterion for planetesimals, which is derived from the condition in which the contraction timescale is shorter than the diffusion timescale. The collapse criterion $t_{\rm contr} < t_{\rm diff}$ is then

$$\frac{v_{\rm rms,cl}^2 R_{\rm cl}}{3GM_{\rm cl}} \sim \alpha_{\rm vir}/15 < 1, \tag{2.12}$$

where we define $\alpha_{\rm vir} \sim (5v^2_{\rm rms,cl}R_{\rm cl})/(GM_{\rm cl})$ as the virial parameter for a spherical clump (e.g., Bertoldi & McKee, 1992) that is gravitationally bound when $\alpha_{\rm vir} \leq 1$. This condition also guarantees collapse against turbulent diffusion from Equation 2.12. If $\alpha_{\rm vir} > 1$, however, the dust particles have enough kinetic energy to expand through the gas.

If a clump is stable against turbulent diffusion, it may still be tidally sheared apart in the protoplanetary disk. Gerbig et al. (2020) defines the condition for stability against tidal shear to be that the clump's self-gravity is larger than the tidal acceleration in three-body dynamics:

$$\frac{GM_{\rm cl}}{R^2_{\rm cl}} > 3\frac{GM_*}{r^2_{\rm d}}\frac{R_{\rm cl}}{r_{\rm d}} \implies M_{\rm cl} > 3M_*\left(\frac{R_{\rm cl}}{r_{\rm d}}\right)^3, \tag{2.13}$$

where $r_{\rm d}$ is the orbital distance of the dust clump.

2.5 Related Studies

Before presenting our work, we will first offer a brief review of related studies which also explore dust particle trapping and planetesimal formation in protoplanetary disks using multi-dimensional hydrodynamics codes. Carrera et al. (2021) present the first 3D simulations of planetesimal formation in the presence of a pressure bump modeled specifically after those observed by ALMA. The authors conduct a series of 3D shearing box simulations using ATHENA gas+particle code (not publicly available), an Eulerian (grid-based) code. The code is run in pure hydrodynamic mode with particle feedback and

particle self-gravity, implemented using a particle-mesh approach. In these simulations, a pressure bump is placed at the center of the box, along with an initial solid-to-gas ratio of $Z = 0.01$. They conduct a total of nine simulations varying several parameters, in particular the pressure bump amplitude and the dust grain size.

Carrera et al. (2021) find that for centimeter-size particles, pressure bumps reliably create the conditions necessary to trigger planetesimal formation by the SI, even for smaller amplitude bumps where there is no particle trap (a particle trap means that particle drift is halted). They also find that removing particle feedback significantly delays the particle accumulation and planetesimal formation, and ultimately conclude that planetesimal formation in pressure bumps relies on SI and not only pure GI due to concentration. However, the results for smaller millimeter-size particles were inconclusive, which is a significant limitation because the maximum particle sizes that we observe in ALMA rings are ∼millimeter-sized. Therefore, Carrera & Simon (2022) extends on this work by running a new high-resolution simulation with millimeter-size grains and a large pressure bump. The objective is to determine whether the SI can form planetesimals in a pressure bump out of millimeter-size grains.

Carrera et al. (2021) note that clumping by SI only seems to be an efficient process when the dust-to-gas ratio Z has already reached some minimum threshold, and that it is more efficient when the headwind Π induced by the pressure gradient is lower (e.g., Bai & Stone, 2010). As shown in Sekiya & Onishi (2018), the overall clumping structure of the particle

filaments produced by the SI scales with Z/Π, which allows Carrera & Simon (2022) to rescale the strong clumping criteria of Li & Youdin (2021) for any pressure profile. They report that, although the Z/Π value they measure is well above the critical limit where previous studies found clumping would occur, they did not observe any strong clumping nor planetesimal formation. This is likely because the region with high Z/Π is narrow and the particle crossing time across this region is shorter than the growth timescale of the SI. Therefore, this introduces an additional criterion, which is that the time particles spend within a high-Z/Π region must be long enough to allow the SI to develop filaments. Thus, the possible pathways to planet formation are significantly limited by this result, indicating that either protoplanetary disks routinely form centimeter-sized grains or the model that planetesimals form when a pressure bump triggers the SI is incorrect. Either way, further investigations are required of both the theory and numerical work behind these simulations.

We emphasize that the work presented in this thesis is not intended to be a follow up to the work by Carrera et al. (2021) and Carrera & Simon (2022). Instead, we present their work here to offer valuable context on the current scope of studies and simulations being conducted in this field. Their work is capable of directly simulating fragmentation and formation of bound clumps by gravitational collapse, whereas our simulations do not have sufficiently high resolution to achieve this, as it becomes too computationally costly. Instead, we are only reporting on the general dust-gas dynamics inside a pressure bump generated by a planet. We are, however, using the first publicly available code that supports

self-gravity, which, again, is not necessary for initial dust clumping to occur, but is required to keep the clump intact against tidal shearing over time. So, future work may build off of the results presented here to further investigate the ability of these pressure bumps to form and maintain bound dust clumps.

Chapter 3

Methods

3.1 Numerical Methods

The code we are using to perform the simulations is GIZMO, a flexible, massively-parallel, multi-physics code, presented in Hopkins (2015). Although originally designed for large scale cosmological simulations, we choose to use GIZMO because it is the only publicly available hydrodynamics code that supports self-gravity for both dust and gas particles, which is necessary for directly simulating dust clumping that is then stable against tidal shear. The numerical method used for the hydrodynamics is the Lagrangian "meshless finite mass" (MFM) method, which has been validated in various studies using a series of benchmark tests and comparisons (e.g., Hopkins & Raives, 2016; Hopkins, 2016, 2017; Su et al., 2017). Several standard hydrodynamic tests performed are the Sod shock tube and

Kelvin-Helmholtz instability, showing MFM's excellent agreement with analytical solutions. The MFM formulation conserves particle masses by eliminating mass fluxes between particles, i.e., no mass flux across the particle faces. The volume partition of the particles is determined by the weighted kernel at each point corresponding to the location of the particle. This is similar to a Voronoi tessellation, but with the boundaries smoothed. The fluid equations are then solved by integrating over the domain of each particle/cell. MFM belongs to the category of arbitrary Lagrangian-Eulerian finite volume Godunov methods and is most closely related to Voronoi-based moving-mesh methods. In the MFM method, the "particles" are actually just moving cells representing a finite volume, with a well-defined volume partition. The equations used in these methods are derived from explicit volume integrals (Hopkins, 2015).

Smoothed Particle Hydrodynamics (SPH) (described in, e.g., Monaghan, 1992, 2005; Liu & Liu, 2010) is another particle-based computational method used to simulate fluid flows. It is a mesh-free, Lagrangian technique that represents fluids with particles carrying properties such as mass, position, and velocity. These particles move with the fluid flow, simplifying the tracking of interfaces and boundaries. SPH uses smoothing kernels to interpolate physical quantities over neighbouring particles, ensuring a smooth representation of the fluid. This method is well-suited for problems with complex geometries and free surfaces.

SPH has several limitations, however, which MFM addresses, improving accuracy, stability, and computational efficiency. As mentioned above, the equations used in MFM

are derived from explicit volume integrals, and an important consequence of this is that the MFM method is second-order consistent, while SPH is not even zeroth-order consistent. N-th order consistency refers to the rate at which the error in a numerical approximation decreases as the discretization parameter (e.g., particle spacing h) is refined, or in other words, as the particle resolution is increased. The error in the approximation of quantities like density, pressure, and velocity fields decreases at a rate $O(h^n)$, so these quantities become more accurate at a predictable and quantifiable rate. MFM also better handles boundary conditions and reduces inaccuracies near solid boundaries. By using adaptive algorithms, MFM mitigates issues related to kernel choice and smoothing length, reducing numerical artifacts like particle clustering. It enhances the treatment of incompressibility and stability, reducing reliance on artificial viscosity and providing more realistic fluid behavior. MFM also has superior shock-capturing capabilities and improves consistency and convergence through adaptive particle management, ensuring higher accuracy in long-term simulations and regions with steep gradients. These advancements make MFM a more robust and accurate approach for fluid dynamics problems.

GIZMO also supports the inclusion of multiple species, allowing us to investigate the dust-gas dynamics. The dust particles are integrated using a super-particle method, where each 'super-particle' represents an ensemble of grains with similar properties, such as size, mass, and velocity. The effect of the drag force exerted by the dust on the gas, known as dust 'back-reaction', is also accounted for in the simulations as in Moseley et al. (2019) and

Seligman et al. (2019), using a two-fluid approach where gas and dust are treated as coupled fluids. The drag force between gas and dust, based on their relative velocities, is calculated. Adaptive resolution methods ensure high accuracy in regions with significant dust-gas interactions, and advanced numerical solvers handle the coupled equations of motion, maintaining stability and accuracy over long simulation periods. These methods ensure self-consistent feedback between dust and gas, capturing their mutual influence accurately. Validation against analytical solutions and observational data confirms the accuracy and realism of the simulations.

3.2 Problem Setup

In this section, we present the two problem setups for our simulations; the first is for the 2D global protoplanetary disk simulation, and the second is for the 3D local shearing-box simulation.

3.2.1 2D Global Protoplanetary Disk

Initial Conditions

The protoplanetary disk is modelled as a gas disk around a solar mass star, with an inner radius of 0.2 and an outer radius of 4.0 (unitless values which can be scaled to any appropriate disk size). All values are scaled such that $M_{\odot} = 1$. The Keplerian orbital frequency, gas

sound speed, and gas scale height, temperature, and surface density at the reference radius $r_0 = 1$ are as follows; $\Omega_{K,0} = 1$, $c_{s,0} = 0.05$, $H_0 = 0.05$, $T_0 = 0.0025$, and $\Sigma_0 = 8.84 \times 10^{-4}$. In physical units, taking $r_0 = 1$AU, these values correspond to $\Omega_{K,0} = 2 \times 10^{-7}\text{s}^{-1}$ (i.e. a period of ~ 365 days), $c_{s,0} = 1500$m/s, and $T_0 = 270$K.

The gas in the disk is governed by the following equations for conservation of angular momentum (in polar coordinates) which describe the radial and azimuthal motion, respectively:

$$\frac{\partial}{\partial t}(\Sigma r^2 \Omega_{\text{gas}}) = -\frac{1}{r}\frac{\partial}{\partial r}(\Sigma u_r r^3 \Omega_{\text{gas}}) + \frac{1}{r}\frac{\partial}{\partial r}(\nu \Sigma r^3 \frac{d\Omega_{\text{gas}}}{dr}), \tag{3.1}$$

and

$$\frac{u_\phi^2}{r} = \frac{GM_*}{r^2} + \frac{H}{\Sigma}\frac{dP}{dr}, \tag{3.2}$$

where u_r and u_ϕ are the radial and azimuthal velocities of the gas, Σ is the gas surface density, and $\nu = \eta_{visc} H/\Sigma$ is the kinematic viscosity with dynamic viscosity parameter η_{visc} to be set in the code. Under the viscous α-disk model presented in Shakura & Sunyaev (1973), the gas viscosity is adopted from the $\alpha-$prescription $\nu = \alpha c_s H$, where α is the dimensionless viscosity parameter (usually prescribed a maximum value of $\alpha \lesssim 10^{-3}$ (e.g., Flaherty et al., 2017), although it is highly uncertain). In a steady-state disk, the inward radial velocity of the gas is given by $u_r = -\frac{3\nu}{2r}$, derived by combining the angular momentum conservation and mass conservation of a viscously accreting disk. The mass accretion rate

through the disk is spatially and temporally constant, and is given by

$$\dot{M} = 2\pi\Sigma r u_r = -3\pi\Sigma\nu = \text{constant}. \tag{3.3}$$

Note that $\dot{M} < 0$ implies an inward accretion.

Both observational evidence and theoretical models of protoplanetary disks suggest that their density and temperature profiles typically follow a power-law distribution with radius. We use a radial gas surface density profile $\Sigma \propto r^{-1}$, with a total disk gas mass of $0.01 M_\odot$. The r^{-1} surface density profile is supported by several empirical observations. Zhang et al. (2017) present the first partially spatially resolved observations of the $^{13}C^{18}O$ $J = 3-2$ line emission, a gas tracer that probes the bulk mass distribution, in the closest protoplanetary disk, TW Hya. They report a gas mass distribution scaling of $r^{-0.9^{+0.4}_{-0.3}}$. Zhang et al. (2021) present high-resolution observations of CO isotopologue lines, providing analysis for observations of five protoplanetary disks. From their best-fit disk model parameters, they find the gas surface density exponent to be -1 for four of the disks, and -0.8 for the other.

The r^{-1} density scaling then also implies $\nu \propto \Sigma^{-1} \propto r$, with α usually being a spatially constant value. However, η_{visc} is currently a parameter set in the code and is spatially (and temporally) constant, which implies that $\nu \propto r^{9/4}$ and $\alpha \propto r^{5/4}$, but we plan to implement a more physically realistic profile in the future. In the code, we set $\eta_{visc} = 3.305 \times 10^{-8}$ in code units, so at $r_0 = 1.0$, $\alpha = 4.42 \times 10^{-5}$. We choose a low α compared to the usual

$\alpha = 10^{-3}$ prescription, because using a value for η_{visc} that is even one order of magnitude higher significantly slows the simulation runtime.

The radial gas temperature profile we use is $T \propto r^{-\frac{1}{2}}$. The following derivation considers the main source of heating to be irradiation by the star, and provides the motivation behind this choice of temperature profile. The flux from stellar radiation is

$$F_*(r) = \frac{L_*}{4\pi r^2}, \tag{3.4}$$

where L_* is the luminosity of the star. But considering that the irradiating flux is the projection of this flux onto the surface of the disk, we have

$$F_{irr}(r) \approx \phi \frac{L_*}{4\pi r^2}, \tag{3.5}$$

where ϕ is the shallow grazing angle that the stellar light can illuminate. The irradiation heating of the disk (for the two sides) is then

$$Q_+^{irr} = \phi \frac{L_*}{2\pi r^2}. \tag{3.6}$$

We assume that the disk's effective temperature is exactly enough to radiate this heating

away, and assuming the disk to be optically thick (i.e., radiating as a blackbody), we have

$$2\sigma_{SB}T_{\text{eff}}^4 = \phi\frac{L_*}{2\pi r^2} \implies T_{\text{eff}} = \left(\phi\frac{L_*}{4\pi\sigma_{SB}r^2}\right)^{1/4} \propto r^{-1/2}, \tag{3.7}$$

where σ_{SB} is the Stefan-Boltzmann constant.

Another possible heating source is viscous heating due to the accretion process, which results in a temperature scaling $T_{\text{eff}} \propto r^{-3/4}$ in the α-disk model (Shakura & Sunyaev, 1973). Since T_{eff} from viscous accretion drops off at a steeper rate than from irradiation by the star, T_{eff} is dominated by irradiation at large r, so we will consider irradiation to be our main source of heating. Furthermore, Chiang & Goldreich (1997) explore the role of stellar irradiation and vertical disk structure, finding that the disk's absorption and re-emission of stellar radiation contributes to the observed temperature distribution. D'Alessio et al. (1998) supported these findings with detailed simulations that incorporate both radiative transfer and thermal balance, finding that a $r^{-\frac{3}{7}}$ scaling emerges as a result of heating through irradiation by the star. Although this is the more realistic scaling profile, $-3/7$ is very close to our derived $-1/2$, so we choose to use the simpler $r^{-\frac{1}{2}}$ scaling.

The gas sound speed then scales as $c_s = \sqrt{\frac{k_B T(r)}{\mu m_{\text{H}}}} \propto T^{\frac{1}{2}} \propto r^{-\frac{1}{4}}$, where k_B is the Boltzmann constant, μ is the mean molecular weight, and m_{H} is the mass of a hydrogen atom (normalized to 1 in code units). The Keplerian orbital frequency scales as $\Omega_K \propto r^{-\frac{3}{2}}$, so that the gas scale height scales as $H = \frac{c_s}{\Omega_K} \propto r^{\frac{5}{4}}$. All our calculations consider a viscous gas described by the

ideal gas equation of state $P = \rho c_s^2$, with the volume density $\rho = \frac{\Sigma(r)}{H(r)} \propto r^{-\frac{9}{4}}$. This results in the gas pressure profile scaling as $P \propto r^{-\frac{11}{4}}$, causing an outward pressure gradient force acting on the gas, so the gas orbits the central star at sub-Keplerian velocities. Accordingly, the gas particles' initial velocity is set as

$$u_\phi = \Omega_{\text{gas}} \cdot r = (\Omega_K^2 r^2 - \frac{11}{4} T_0 r^{-\frac{1}{2}})^{1/2}, \tag{3.8}$$

where the gas temperature $T_0 = 0.0025$ at $r_0 = 1$. The temperature profile is kept constant throughout the runtime of the simulation in order to reduce numerical errors from the hydrodynamics. When the temperature was allowed to evolve based on the hydrodynamic solution found by the code, it caused a steep nonphysical temperature gradient near the inner radius of the disk, leading to nonphysical behaviour of the gas. This is due to the void of particles at the center of the disk, which does not properly capture the physics near the inner disk region.

We form the initial protoplanetary disk using concentric rings of gas particles. These particles are evenly distributed around each ring, and each ring is radially spaced by $dr = 0.1H(r)$. As such, the spacing between rings increases with orbital distance, scaling with $dr \propto r^{\frac{5}{4}}$. If the mass per gas particle $m_{i,\text{gas}}$ is kept constant throughout the disk, then the number of particles per ring scales as $N_{1D,\text{gas}}(r) \propto r^{\frac{5}{4}}$. This results in a high number of particles per ring in the outer regions of the disk, which consequently increases the resolution

and hence, runtime. To offset this effect, $m_{i,\mathrm{gas}}$ is varied to increase with radius so that there is an equal number of particles per $\log(r)$. This ensures that the resolution does not become unnecessarily high at the outer region of the disk, while the resolution at the inner region can still remain appropriately high. Specifically, the inner ring has $N_{1D,\mathrm{gas}}(r_{\mathrm{in}}) > 128$ and the disk has a total resolution of $N_{\mathrm{total,gas}} \approx 5 \times 10^5$ particles. We achieve convergence at this resolution, as increasing the resolution beyond this point does not significantly alter the root mean square error on u_ϕ and Σ_{gas}, shown in Figure 3.1.

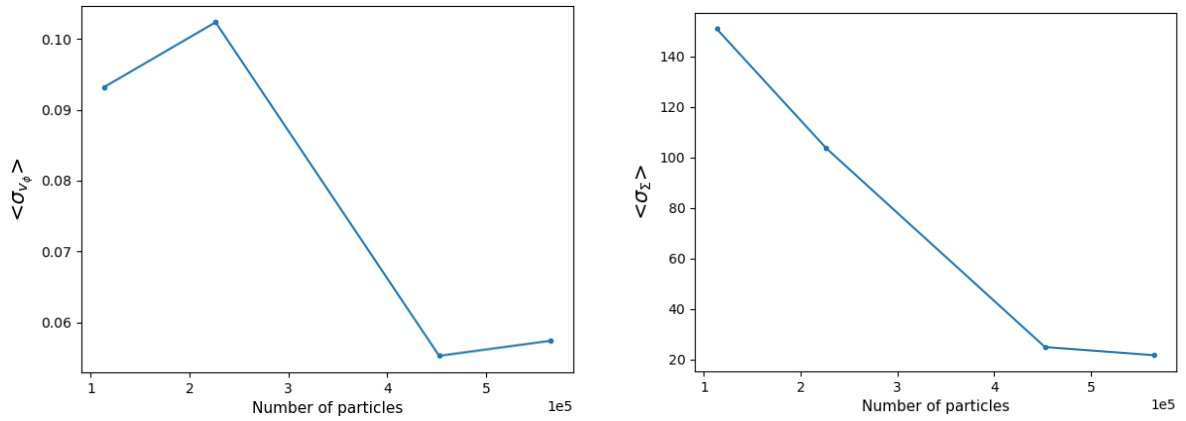

(a) Azimuthal Velocity **(b)** Surface Density

Figure 3.1: Resolution analysis for 2D global disk simulation using root mean square error on (a) azimuthal velocity and (b) surface density. Both plots show convergence around 4.5×10^5 particles.

Boundary Conditions

Initially, the boundary conditions at the inner and outer radius were the combination of a confining term and an additional pressure gradient force. The confining term confines the

particles within the disk so that they cannot flow beyond the set radii by providing a small acceleration kick, defined as follows for the inner boundary:

$$a_\alpha = -x_\alpha \times \left(\frac{r_{\rm cur}}{r_{\rm in}}\right)^2 /(x_0^2 + x_1^2)^{1.5} + \left(x_\alpha \times \frac{r_{\rm in} - r_{\rm cur}}{r_{\rm in}}\right) /(x_0^2 + x_1^2)^{1.5}, \tag{3.9}$$

and for the outer boundary:

$$a_\alpha = -x_\alpha \times \left(1 + r_{\rm cur} - \frac{r_{\rm out}}{\Delta r}\right) /(x_0^2 + x_1^2)^{1.5}, \tag{3.10}$$

where $\alpha = (0, 1, 2) = (x, y, z)$, $r_{\rm cur}$ is the current radial position of the particle and Δr is the radial distance the particle has gone beyond the boundary. The pressure gradient force is to account for the lack of particles at the center and outside of the disk. It is added as an additional term in the particle's acceleration, defined as follows:

$$a_{\nabla {\rm P},\alpha} = \pm \frac{11}{4}(0.05^2) \times x_\alpha /(x_0^2 + x_1^2)^{\frac{5}{4}}, \tag{3.11}$$

where $\pm$ will be $+$ for the inner boundary and $-$ for the outer boundary. This additional term is added for gas particles that are between $r_{\rm in}$ to $r_{\rm in} + 4H_{\rm in}$ and $r_{\rm out} - H_{\rm out}$ to $r_{\rm out}$. $H_{\rm in}$ and $H_{\rm out}$ are the scale heights at the inner and outer radius, respectively.

Currently, the boundary conditions at the inner and outer radii of the disk are inflow (accretion onto the central star) and outflow, respectively. To implement these boundary

conditions, we delete any particles that happen to flow beyond the set inner and outer boundaries, instead of using a prescribed mass loss rate. Due to the void of particles, both at the centre of the disk and outside of the disk, we pad the inner and outer radius with ghost gas particles. Ghost particles are particles that are not treated by the hydrodynamics of the code, but instead follow an analytic solution for a circular orbit around the star at the appropriate sub-Keplerian velocity from Equation 3.8. We calculate the change in azimuthal position $\Delta\phi = \omega \times \Delta t = \frac{u_\phi}{r} \times \Delta t$ to adjust the position of each ghost particle after every timestep Δt. This reduces the effect that the void of particles has on the hydrodynamic solution found by the code, since this sudden lack of particles causes a steep, nonphysical density gradient, and hence pressure gradient, resulting in nonphysical gas dynamics and spurious wave propagation.

3.2.2 3D Local Shearing Box

Initial Conditions

We are investigating the dust-gas dynamics near and at a local pressure perturbation in a gas disk, with the inclusion of both dust self-gravity and dust 'back-reaction'. The pressure perturbation is established by a tidal interaction with an embedded planet (as described in Section 2.2). For our 3D simulation, we focus on the local dynamics using a 'shearing-box' approximation, which means the calculations are carried out on a small Cartesian section of the disk within a rotating frame centered at $(r_0,\ \phi_0 + \Omega_0 t,\ z_{\rm mid})$, where $\Omega_0 = \Omega(r_0)$

represents the Keplerian orbital frequency at r_0, and $z_{\rm mid}$ is the coordinate of the disk midplane. In this frame, the local Cartesian coordinates are given by $\boldsymbol{x} = (x, y, z) = (r - r_0, r_0(\phi - \phi_0) - r_0\Omega_0 t, z)$. The momentum equation for gas is then

$$\frac{D\boldsymbol{u}}{Dt} = -\frac{\nabla P}{\rho} - 2\Omega_0 \hat{\boldsymbol{z}} \times \boldsymbol{u} + 3\Omega_0^2 \boldsymbol{x} - \Omega_0^2 \boldsymbol{z} + \boldsymbol{a}_{\rm dust} + \boldsymbol{a}_{\rm planet}, \tag{3.12}$$

where $D/Dt = \partial/\partial t + (\boldsymbol{u} \cdot \nabla)$ is the Lagrangian derivative, ρ is the gas density, P is the gas pressure, $\boldsymbol{u}$ is the gas velocity, $\boldsymbol{a}_{\rm dust}$ is the "back-reaction" acceleration, and $\boldsymbol{a}_{\rm planet}$ accounts for the planet's gravitational force, defined below.

First, we will consider the gas particles. The 3D box is set up with a uniform gas density distribution in the azimuthal and radial directions, and a stratified density distribution in the vertical direction, following $\rho \propto \exp(-z^2)$, where z is in units of H. The box has side lengths $L_{{\rm box},x} = L_{{\rm box},y} = 12H$ and $L_{{\rm box},z} = 8H$, with $N_{\rm 1D,gas}^{D-1}(z)$ resolution elements, or gas particles of mass $m_{i,{\rm gas}}$, where D is the number of dimensions. All our calculations consider an inviscid, locally isothermal gas described by the equation of state $P = \rho c_s^2$ (Lee et al., 2022). The initial velocity field is set to the equilibrium solution in the absence of a planet and in the absence of dust "back-reaction":

$$\bar{\boldsymbol{u}} = \left(0, -\frac{3}{2}x\Omega_0 - \eta U_K, 0\right) = \left(0, -\frac{3}{2}x\Omega_0 - \Pi c_s, 0\right), \tag{3.13}$$

where $U_K = \Omega_0 r_0$ is the Keplerian velocity at the center of the simulation box, $\eta \equiv \eta(r =$

$r_0) = -(\partial P_0(r)/\partial r)/(2\rho_0\Omega^2 r)$ is the usual dimensionless pressure support parameter, $P_0 = P_0(r_0)$ is the unperturbed gas pressure evaluated at the center of the simulation box, and $\Pi \equiv \eta(U_k/c_s)$.

Next, we consider the dust particles. The dust "super-particles" are spawned at a constant rate from a 2D particle spawning mesh at the right edge $+\hat{\boldsymbol{x}}$ of the box. Dust grains enter the right side of the box at $+\hat{\boldsymbol{x}}$ (i.e., $r > r_0 + L_{\rm box}/2$) and exit the left side of the box at $-\hat{\boldsymbol{x}}$ (i.e., $r < r_0 - L_{\rm box}/2$). The dust spawning mesh has the same vertical distribution as the gas density, and is uniformly distributed in the azimuthal direction with a particle resolution of $N_{\rm 1D,gas}(z)$. We set the mass of the dust particles to be $m_{i,\rm dust} = 0.01 m_{i,\rm gas}$. The particles are spawned at a constant rate, set to the equilibrium drift:

$$\bar{\boldsymbol{v}} = \bar{\boldsymbol{u}} - (2\tau_S, \tau_S^2, 0)\Pi c_s/(1+\tau_S^2), \tag{3.14}$$

so that the steady-state dust-to-gas ratio in the box *without* a bump is $\langle \mu_0 \rangle = 0.01$.

The dust grains drift radially inwards with a drift velocity that is dependent on the input parameter τ_S. We focus on smaller grains with $\tau_S = 0.1$. In general, we only plan to focus on grains with $\tau_S = 0.01 - 1$, because when $\tau_S > 1$, the dust grains are essentially decoupled from the gas, so there is no physically reasonable size of pressure bump that can trap the

dust. The momentum equation for dust particles is

$$\frac{d\boldsymbol{v}}{dt} = -\frac{\boldsymbol{v}-\boldsymbol{u}}{t_s} - 2\Omega_0\hat{\boldsymbol{z}}\times\boldsymbol{v} + 3\Omega_0^2\boldsymbol{x} - \Omega_0^2\boldsymbol{z}, \tag{3.15}$$

where $\boldsymbol{v}$ is the dust particle velocity, $d\boldsymbol{v}/dt$ is its Lagrangian derivative. The simulation is run with no dust until the gas distribution reaches a steady-state. We determine this point to be when the amplitude of the pressure bump established by the planet no longer varies with time, at which point dust spawning is turned on.

Finally, we will consider the gravitational effect of a planet of mass M_p located at $\boldsymbol{x_p} = (x_p, y_p, z_p)$ on the gas. We use a planet to establish and enforce the pressure bump in our simulations, and the planet's mass controls the shape of the resulting bump. Lee et al. (2022) find that pressure bumps form when $M_p \geq 0.5M_{\rm th}$. We use $M_p = 0.5M_{\rm th}$, because we find that higher mass planets engulf nearly all the gas in the shearing box. We place the planet at the midplane in the center of the box. Since the governing equations are solved with respect to the center of the shearing-box, placing the planet at the center simplifies our analysis of the fluid flow with respect to the planet. Placing the planet at the center of the box also allows enough space (6H) to the right of the planet for the pressure bump to form. The planet's gravitational potential is given by

$$\Phi_p = -\frac{GM_p}{\sqrt{(x-x_p)^2 + (y-y_p)^2 + (z-z_p)^2 + r_s^2}}, \tag{3.16}$$

where the smoothing length parameter $r_s = 0.1$. The planet's gravitational potential is accounted for in Equation 3.12 by $\boldsymbol{a}_{\text{planet}}$, defined as

$$\boldsymbol{a}_{\text{planet}} = 2\Pi c_s \Omega_0 \hat{\boldsymbol{x}} - \nabla \Phi_p, \tag{3.17}$$

where the first term on the right hand side also accounts for the acceleration due to the large-scale gas pressure gradient. The pressure discontinuity between the $\pm\hat{\boldsymbol{x}}$ boundaries is not otherwise allowed in shear-periodic boundaries.

Boundary Conditions

The boundary conditions for the gas are periodic in the azimuthal (y) direction and outflow in the vertical (z) direction. The boundary condition in the radial (x) direction is periodic, but we impose killing zones along the x boundaries where the velocity is gradually damped back to its initial condition in order to damp out spurious waves propagating radially through the gas. The damping helps to minimize the boundary effects, and is particularly important for periodic boundary conditions because any waves propagating radially will loop back through the box, which is an artificial effect and can cause nonphysical behaviour. The damping condition is given by the following expression from Fung & Ono (2021):

$$\frac{\partial u_\alpha}{\partial t} = (u_{\alpha,0} - u_\alpha) \sin^2 \left(\frac{\pi}{2} |x - x_{\text{kill}}| \right), \tag{3.18}$$

where u_α are the components of the particle's velocity, with $\alpha = (x, y, z)$, $u_{\alpha,0}$ is the initial velocity at t=0, x is the radial position of the particle, and x_{kill} is $-\hat{x} + 0.6H$ and $+\hat{x} - 0.6H$ for the inner and outer radial boundaries, respectively. The width of the boundary was taken to be $0.05 L_{\text{box,x}} = 0.05 \times 12H = 0.6H$. This value was chosen to be a small enough fraction of the box's radial size so as not to significantly affect the physics in the main simulation box, while also being large enough to have enough particle resolution. In future work, we intend to experiment with this choice by varying the value and investigating its effect on the results.

Chapter 4

Results

4.1 2D Global Protoplanetary Disk

As we are still in the process of code development for the 2D global disk simulation, we will present the progression of the simulation results thus far. We will highlight the effect of various boundary conditions and parameters on the behaviour and evolution of the gas disk and its properties, including surface density, velocity and acceleration, summarized in Table 4.1. Figure 4.1 shows the global protoplanetary disk. The goal of varying the boundary conditions is to determine an appropriate disk setup that will allow us to achieve a certain target precision of the desired solution. Our target precision is dependent on the scale of the subsonic turbulence, which is the source of viscosity in the disk. The kinematic viscosity is

given by

$$\nu = \alpha c_s H = \alpha c_s^2/\Omega \implies \nu\Omega = \alpha c_s^2, \tag{4.1}$$

so that the turbulent velocity, length scale, and acceleration are parameterized by

$$[\nu\Omega] = [\sigma^2] = [\frac{L^2}{T^2}] \implies \sigma = \sqrt{\alpha} c_s, \tag{4.2}$$

$$[\frac{\sigma}{\Omega}] = [l] = [L] \implies l = \sqrt{\alpha}\frac{c_s}{\Omega} = \sqrt{\alpha} H, \tag{4.3}$$

$$[\sigma\Omega] = [\delta a] = [\frac{L}{T^2}] \implies \delta a = \sqrt{\alpha} c_s \Omega, \tag{4.4}$$

respectively. We can also relate the surface density to α through $\frac{\Delta\rho}{\rho} = \mathrm{Ma}^2 = \left(\frac{u_g}{c_s}\right)^2 \propto \alpha$, where Ma is the mach number, and $\Sigma = \rho H$, so then the error on Σ is given by

$$\delta\Sigma = \sqrt{(\Delta\rho)^2 + (\Delta H)^2} \propto \sqrt{\alpha^2 + \alpha} \propto \sqrt{\alpha}, \tag{4.5}$$

since $\sqrt{\alpha}$ dominates for $\alpha < 1$. All properties are then characterized by $\sqrt{\alpha} \sim 0.03$ for a typical $\alpha \sim 10^{-3}$. So, we are aiming to achieve variations in velocity, acceleration, and surface density on an order of magnitude below this value. We will now present the test cases that have been run thus far, showing the results for these disk properties.

Test 1: Initially, the simulations were run with no viscosity and no boundary conditions, shown in Figure 4.2. The particles near the outer edge of the disk are then able to flow

Test	Fig.	Boundary Condition	Disk Properties	Results
1	4.2	None	Inviscid, $r_{\text{out}} = 2.0$	Outwards spreading in outer disk region. Indefinite expansion of disk causes a nonphysical density profile.
2	4.3	Inner+Outer: confining term and extra pressure gradient force	Inviscid, $r_{\text{out}} = 2.0$	Particles cannot flow beyond inner and outer boundaries. Cause gas particle pile up at inner radius.
3	4.4	Inner: Inflow, Outer: confining term and extra pressure gradient force	Inviscid, $r_{\text{out}} = 2.0$	Similar results to test 2, but reduces further potential wave propagation/reflection at inner radius, so we keep inflow.
4	4.5	Inner: Inflow, Outer: confining term and extra pressure gradient force	Viscous, $r_{\text{out}} = 2.0$	Smoother gas density distribution, e.g., smaller gas perturbation near inner edge. Slight gas pile up at outer radius due to viscous spreading + confinement.
5	4.6	Inner: Inflow, Outer: confining term and extra pressure gradient force (smaller boundary width)	Viscous, $r_{\text{out}} = 2.0$	Similar to test 5, but with slightly larger gas pile up at outer radius.
6	4.7	Inner: Inflow, Outer: confining term and extra pressure gradient force	Viscous, $r_{\text{out}} = 4.0$, particle mass varied with r	Similar results to test 5, but smoother density profile in the middle region of disk.
7	4.8	Inner: Inflow, Outer: Outflow, both padded with ghost particles	Viscous, $r_{\text{out}} = 4.0$, particle mass varied with r	Mass loss at outer radius due to initial spreading past physical outer radius into ghost particle region. Gas pile ups at inner radius are still occurring.

Table 4.1: Summary of all 2D global disk simulation test cases which were run using different boundary conditions. Column 1: Figure reference. Column 2: Boundary conditions used for the test case. Column 3: Disk properties and parameters used for the test case. Column 4: Summary of the key results and disk behaviour for the test case.

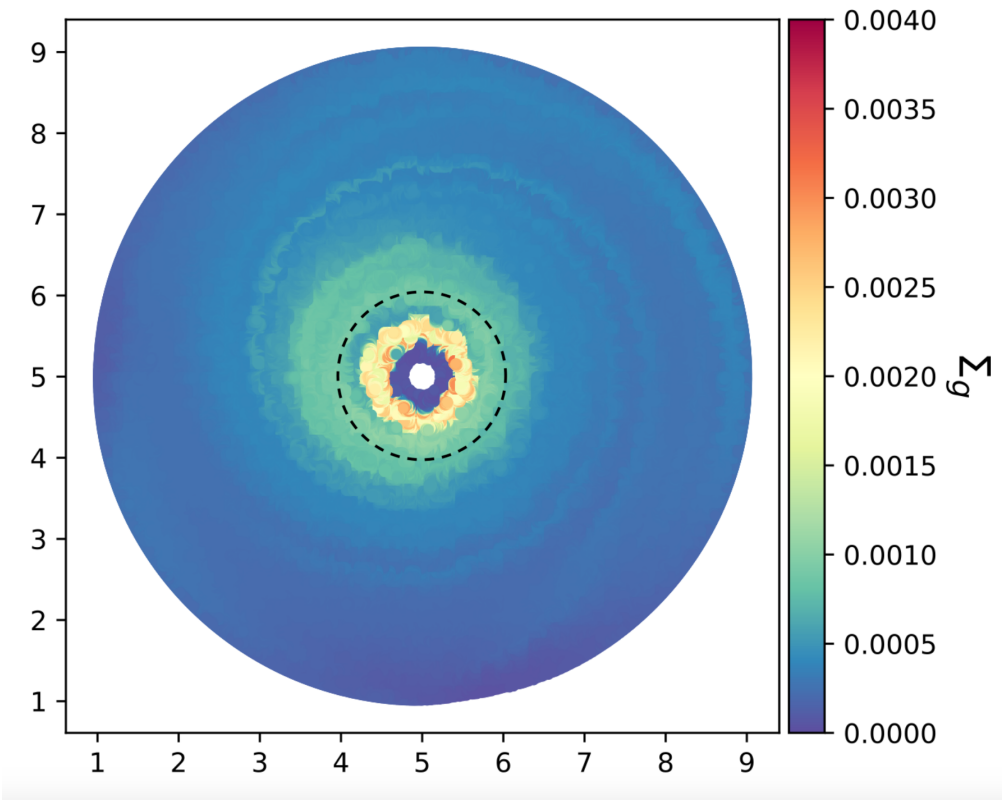

Figure 4.1: Surface density image of the global protoplanetary disk after $356\Omega_{K,0}^{-1}$, where $\Omega_{K,0}^{-1}$ is the orbital period defined at the reference point $r_0 = 1$, identified by the dashed black circle. Disk properties and boundary conditions are those described in Figure 4.8.

outwards indefinitely, and this causes the drop in surface density at the outer radius (see Figure 4.2d). Although some spreading is expected in a viscous disk, this is an inviscid test case, so physically we do not expect to see this behaviour. Since this is a numerical effect which significantly impacts the density distribution, it leads to nonphysical behaviour and we lose too many particles at the outer edge.

Test 2: The first boundary conditions introduced at the inner and outer radius were a combination of 1) a confining term to keep the particles within the set boundaries, and 2) an

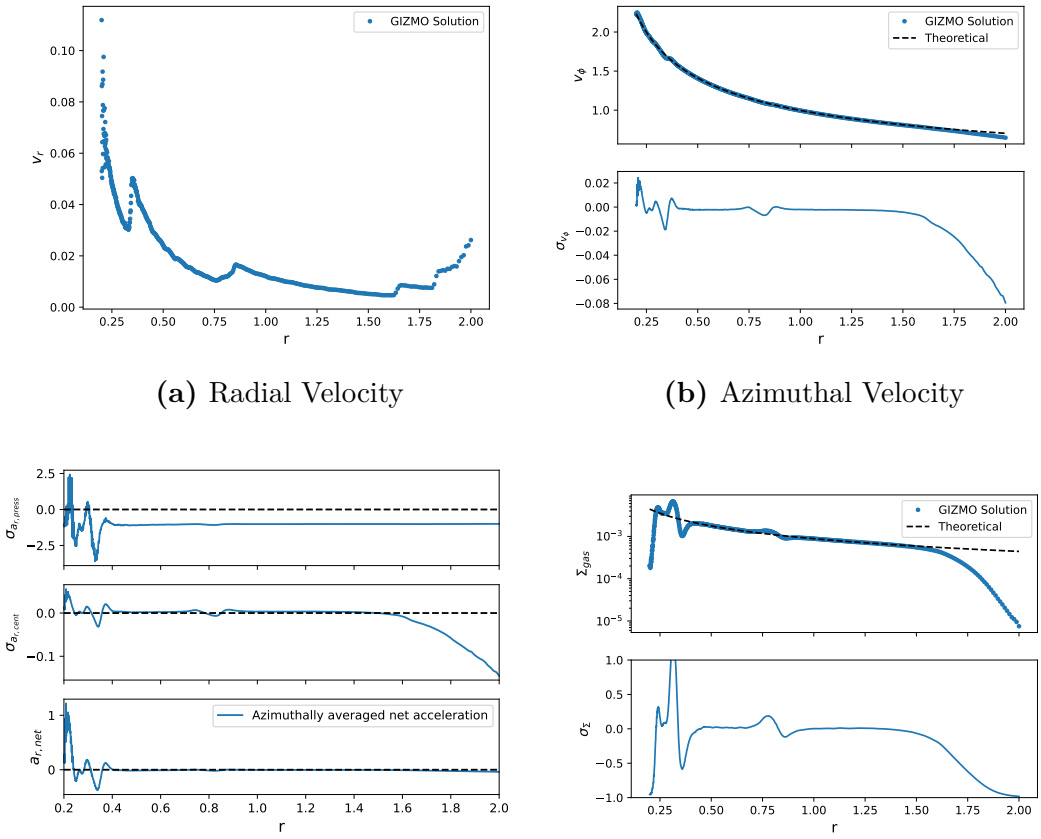

(a) Radial Velocity

(b) Azimuthal Velocity

(c) Radial Acceleration

(d) Surface Density

Figure 4.2: Test 1: No boundary conditions. This is an inviscid disk with outer radius at $r = 2.0$ and constant particle mass. The plots show the results of the evolution of the gas disk after $200\Omega^{-1}$. Plot a) Azimuthally averaged radial gas velocity. Theoretically, for an inviscid disk without numerical errors, $u_r = 0$. Plot b) Azimuthally averaged azimuthal gas velocity (see Equation 3.8 for theoretical u_ϕ). Upper panel: Hydrodynamic GIZMO solution and theoretical solution are plotted. Lower panel: Fractional difference error between the code solution and theoretical solution is plotted. The theoretical solution refers to the initial condition of the disk since, if it were not for numerical errors, the disk should be in steady state and maintain its initial condition exactly. Plot c) Top+Middle panel: Fractional difference error between the code solution and theoretical solution for azimuthally averaged radial acceleration due to the gas pressure gradient force and the centrifugal force, respectively. Bottom panel: Azimuthally averaged net radial acceleration of the gas, which theoretically should be zero. Plot d) Azimuthally averaged gas surface density, with upper and lower panels the same as those described in Plot b. Theoretical solution should follow $\Sigma \propto r^{-1}$ (see Section 3.2.1).

additional pressure gradient force to account for the effect of the particle void at the center and outside of the disk. The details of these two conditions are described in Section 3.2.1. The results are shown in Figure 4.3. These boundary conditions ensure that the particles do not flow beyond the set inner and outer radii. As we see in Figure 4.3d, there is no loss of particles at the outer radius, unlike in Figure 4.2d. We also see a decrease in the error of the net radial acceleration near the inner radius, shown in Figure 4.3c as compared to Figure 4.2c. However, these boundary conditions result in nonphysical behaviour, in particular near the inner region of the disk, because they cause gas particles to pile up, driving spurious waves through the disk.

Test 3: In an attempt to reduce these perturbations in the density profile near the inner edge of the disk, both the confining and additional pressure gradient terms are removed at the inner boundary, and replaced with an inflow boundary condition instead, as described in Section 3.2.1. The results are shown in Figure 4.4. This modification does not significantly impact the density distribution, and we continue to see gas perturbations near the inner edge. However, we choose to keep inflow as the inner boundary condition to reduce potential wave propagation as the disk evolves over longer timescales.

Test 4: We then introduce viscosity with the goal of smoothing out the gas perturbations in the disk using the $\alpha-$disk model (Shakura & Sunyaev, 1973). This is also a more physically accurate model of protoplanetary disks. Figure 4.5 shows the results for a viscous disk with $\eta_{visc} = 3.305 \times 10^{-8}$ in code units, corresponding to $\alpha = 4.42 \times 10^{-5}$ at $r_0 = 1.0$ (see Section

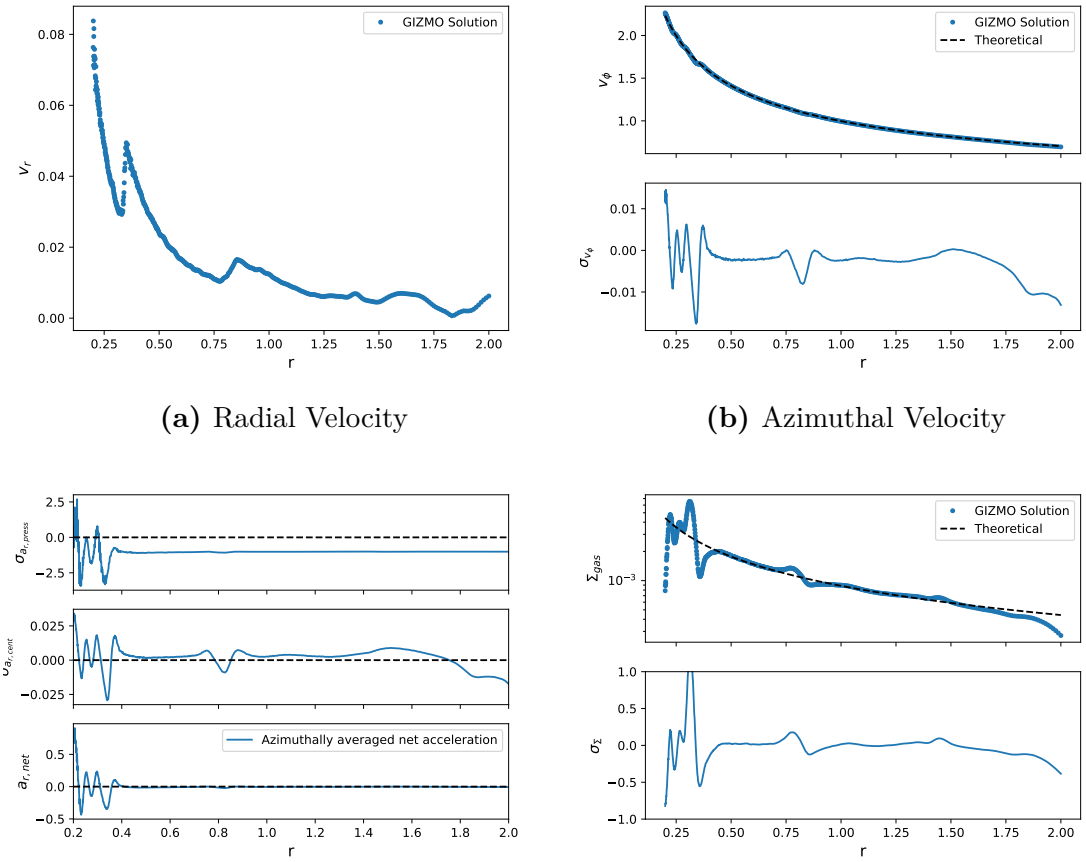

(a) Radial Velocity

(b) Azimuthal Velocity

(c) Radial Acceleration

(d) Surface Density

Figure 4.3: Test 2: Confining term and additional pressure gradient force conditions for both boundaries. This is an inviscid disk with an outer radius at $r = 2.0$ and constant particle mass. The plots shown here are the same as those described in Figure 4.2.

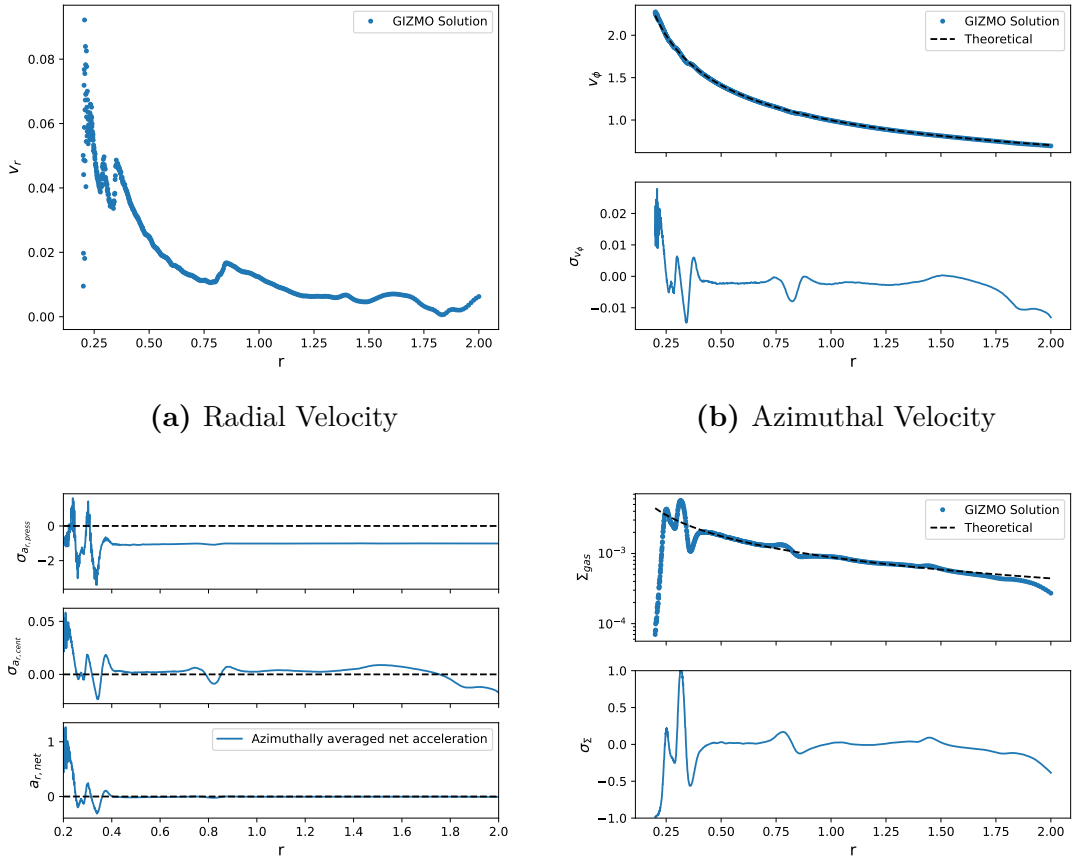

(a) Radial Velocity

(b) Azimuthal Velocity

(c) Radial Acceleration

(d) Surface Density

Figure 4.4: Test 3: Confining term and additional pressure gradient force at outer boundary and inflow at inner boundary. This is an inviscid disk with an outer radius at $r = 2.0$ and constant particle mass. The plots shown here are the same as those described in Figure 4.2.

3.2.1 for details on the chosen viscosity prescription), and the same boundary conditions as in Figure 4.4. We see some smoothing in the gas density distribution (Figure 4.5d) as compared to the inviscid case (Figure 4.4d), in particular the pile ups near the inner radius. Although the outer boundary conditions have not changed, we see a slight gas pile up at the outer edge. This is due to the viscosity causing some spreading in the outer disk region, leading to a pile up where the particles are being confined. However, we choose to keep this confining term at the outer boundary in test 5 and 6 because, otherwise, we lose too many particles from the disk in the outer region as the particles spread outwards indefinitely.

Test 5: In Figure 4.6, the boundary conditions are the same as in Figure 4.5, however the width of the boundary on which the additional pressure gradient force is acting is half the width of that in the previous test case (4.5). We see a slight increase in density at the outer radius (Figure 4.6d), which makes sense since there is less of an inward pressure gradient force acting on the gas at the outer edge to work against the disk spreading.

Test 6: Our goal is to eventually introduce a planet in the disk. The planet's location should be at a radius that is far enough away from each boundary to reduce the boundary effects in the vicinity of the planet, and to leave enough space on the outside of the planet to establish a pressure bump that is also a reasonable distance from the outer edge. Therefore, we then choose to increase the outer radius from $r_{\text{out}} = 2.0$ to 4.0 to allow for more flexibility in the placement of the planet, and to further reduce the boundary effects near the planet and the pressure bump. As described in Section 3.2.1, we also vary the particle mass with

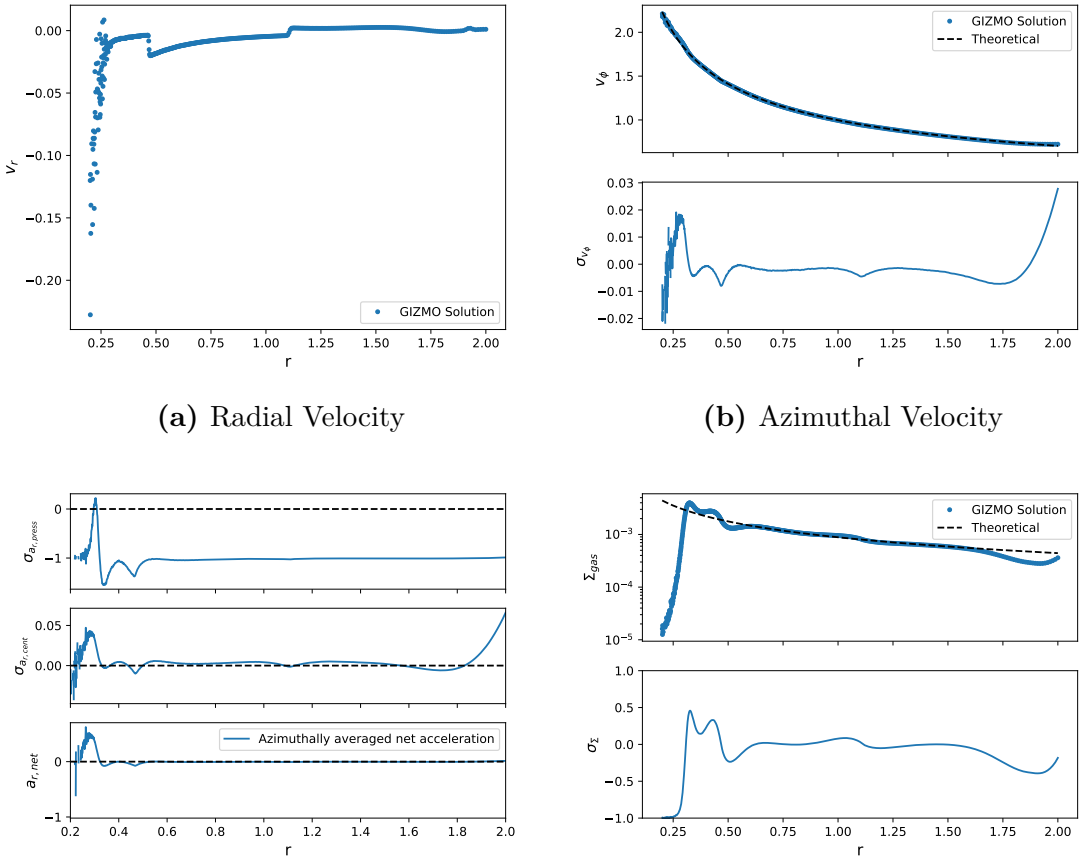

(a) Radial Velocity

(b) Azimuthal Velocity

(c) Radial Acceleration

(d) Surface Density

Figure 4.5: Test 4: Confining term and additional pressure gradient force at outer boundary and inflow at inner boundary. This is a viscous disk with an outer radius at $r = 2.0$ and constant particle mass. The plots shown here are the same as those described in Figure 4.2.

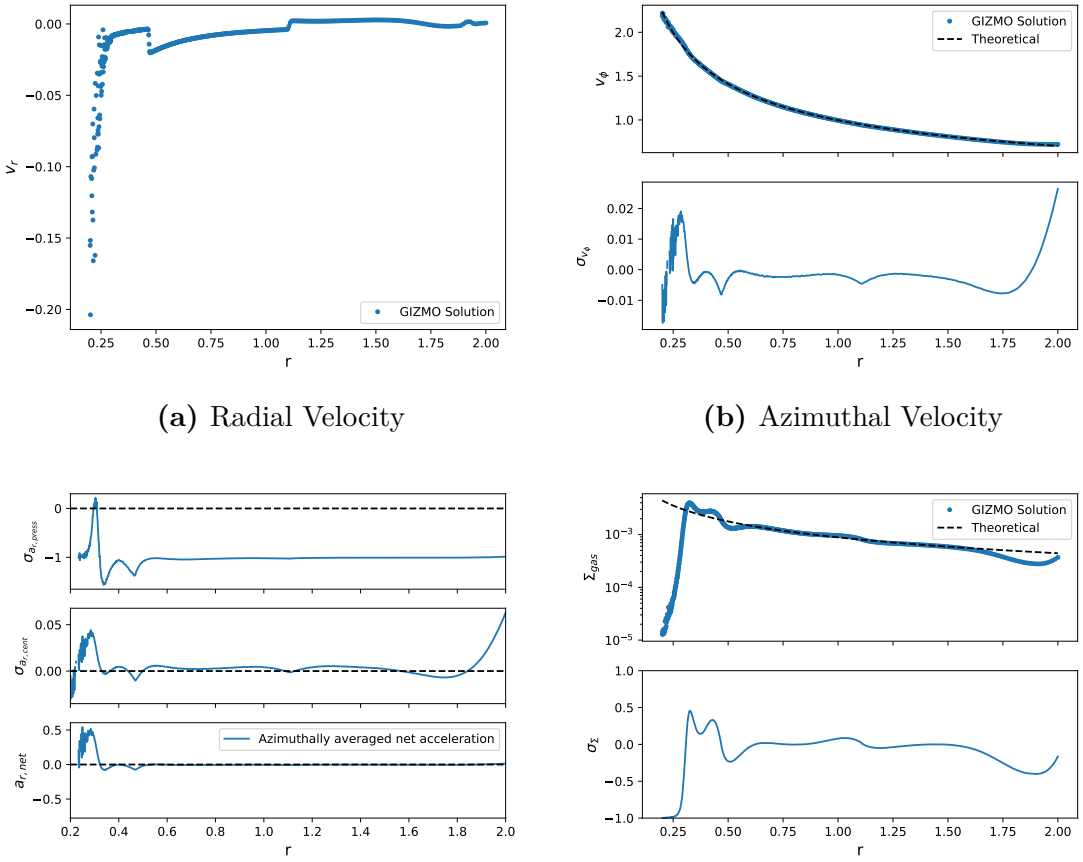

(a) Radial Velocity

(b) Azimuthal Velocity

(c) Radial Acceleration

(d) Surface Density

Figure 4.6: Test 5: Confining term and additional pressure gradient force (with smaller boundary width) at outer boundary and inflow at inner boundary. This is a viscous disk with an outer radius at $r = 2.0$ and constant particle mass. The plots shown here are the same as those described in Figure 4.2.

radius to offset the increase in $N_{\text{total,gas}}$ as we increase the size of the disk. The behaviour of the disk, shown in Figure 4.7, is very similar to the previous test cases, however there is a larger radial width (between $\sim r = 1.0 - 3.0$) that shows smoother behaviour since this region is now further from the boundaries and is less affected by the outer boundary.

Test 7: Finally, in a further attempt to reduce the nonphysical boundary effects, we add ghost particles inside and outside of the disk to pad the inner and outer radius, as described in Section 3.2.1. The boundary conditions used are inflow and outflow at the inner and outer radius, respectively, so that if the gas particles flow into the ghost particle region, they are deleted. The results are shown in Figure 4.8. The radial width of the ring of ghost particles added interior to the inner radius is 0.1 and exterior to the outer radius is 1.0. These ghost particles follow an analytic solution for a circular orbit at the appropriate sub-Keplerian velocity, described in Section 3.2.1, and are not evolved by the hydrodynamic solution of the code. They are intended to lessen the effect of the sudden gap of particles inside and outside of the disk. Figure 4.8d shows a drop in gas density at the outer physical radius ($r_{\text{out}} = 4.0$), due to some initial mass loss from gas particles spreading beyond their physical radial limit into the ghost particle region. There are still pile ups occurring in the inner region, so further test cases will be run in the attempt to mitigate these boundary effects.

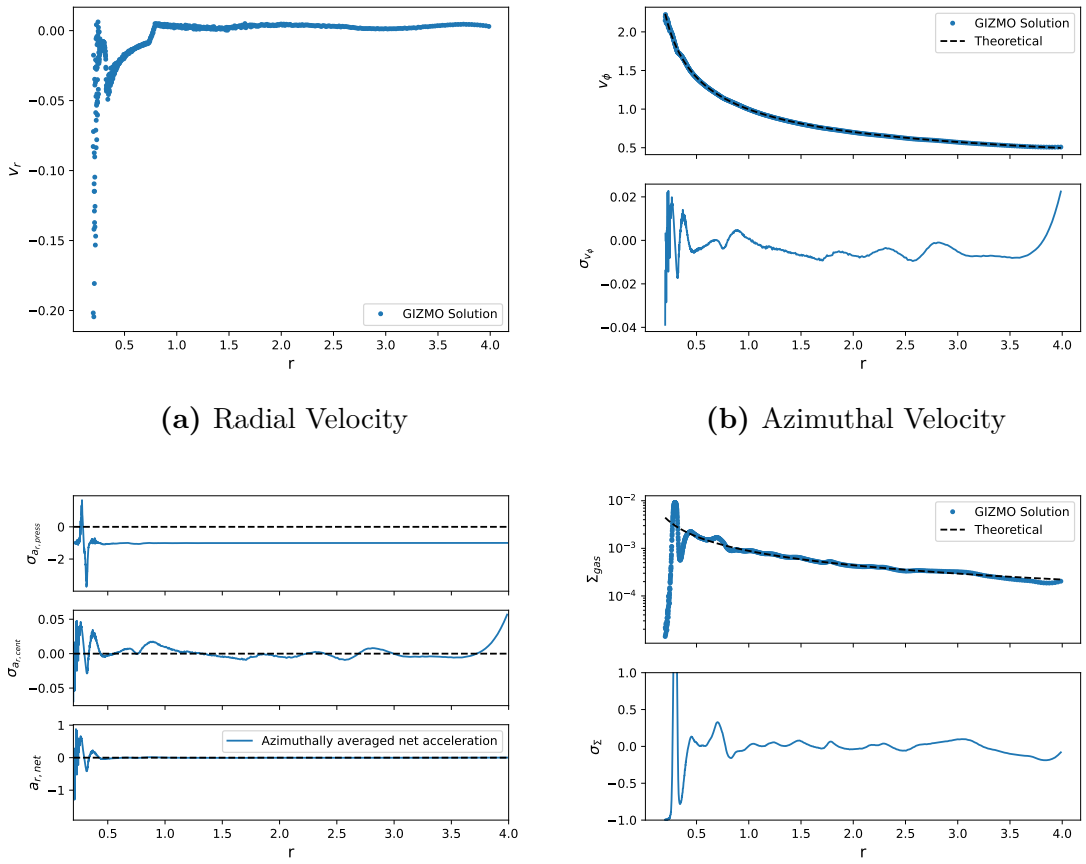

(a) Radial Velocity

(b) Azimuthal Velocity

(c) Radial Acceleration

(d) Surface Density

Figure 4.7: Test 6: Confining term and additional pressure gradient force at outer boundary and inflow at inner boundary. This is a viscous disk with an outer radius at $r = 4.0$, and the particle mass is varied with radius. The plots shown here are the same as those described in Figure 4.2.

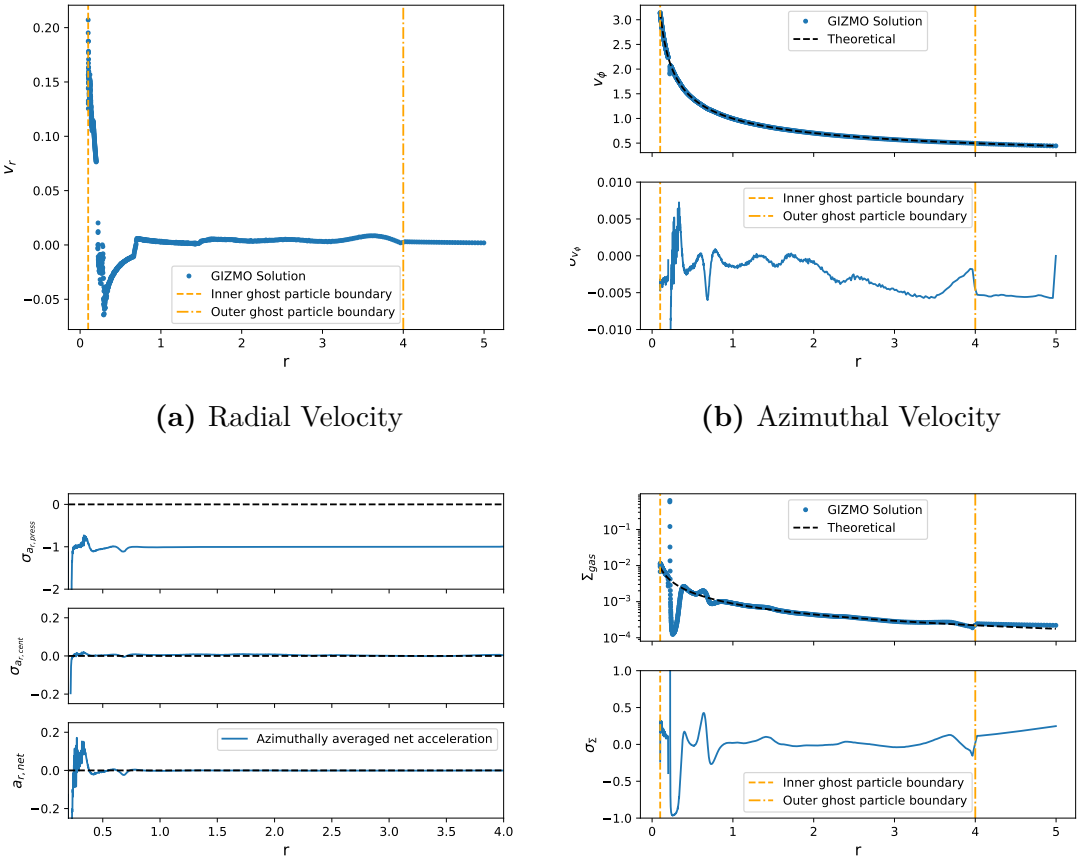

(a) Radial Velocity

(b) Azimuthal Velocity

(c) Radial Acceleration

(d) Surface Density

Figure 4.8: Test 7: Inflow at the inner radius and outflow at the outer radius, which are both padded with ghost particles. This is a viscous disk with an outer radius at $r = 4.0$, and the particle mass is varied with radius. The plots shown here are the same as those described in Figure 4.2.

4.2 3D Local Shearing Box

Next, we present the results thus far from the 3D local shearing box simulations. As described in Section 3.2.2, the simulation is first run with only gas particles before turning on dust spawning. Figure 4.9, 4.10a, and 4.10b visualize the 2D gas density distribution and gas velocity streamlines by taking a slice at the planet location in the $\phi - r$, $z - r$, and $z - \phi$ planes, respectively. The gravity from the planet embedded in the disk causes some of the surrounding gas to be accreted onto the planet, exciting density waves in the gas and pushing the gas away toward the radial boundaries, as discussed in Section 2.2. The result is a density gap around the planet's orbit and a pile up of gas a few H away from the planet, at $x \approx 3H$. In Figures 4.10a and 4.10b, the gas streamlines show both accretion onto the planet, as well as some turbulence in the vertical direction. The expectation in the $z - r$ plane is to see meridional flows (Fung et al., 2015), however turbulence may suppress these flows (Fromang et al., 2011). Turbulence in our simulations may be caused by waves driven through the gas, inducing localized variations in density. This turbulence promotes particle stirring, reducing dust settling onto the midplane and increasing H_{p}. Figure 4.11 shows the radial gas flux in the $z - r$ plane, with slices taken at different ϕ behind, at, and ahead of the planet location. At the planet location (center panel) we see that the flow direction is towards the planet due to the planet's gravitational pull. Further from the planet (azimuthally) we see that the flow direction changes, which may be due to perturbations from the planet driving the gas radially away. Figure 4.12 shows all three components of the gas flux in the $\phi - r$ plane at

the planet location, but as made evident in Figure 4.12b, there appears to be an overly high gas density buildup to the left of the planet, which we will discuss further in Section 5.2.

Figure 4.13a and 4.13b visualize the 2D gas density distribution (background) and the spatial distribution of dust particles (cyan) by taking a slice at the planet location in the $\phi - r$ and $z - r$ plane, respectively, at $350\Omega^{-1}$ after turning on dust spawning for grains with $\tau_S = 0.1$. In Figure 4.14, we observe a pressure bump established by the embedded planet mass before adding dust. The bump is located a few H to the right of the planet. For $\tau_S = 0.1$, we find that the dust particles become trapped slightly outside the center of the bump, around $x \sim 4H$ (Figure 4.13), which differs from expectation based on 2D shearing box simulations (e.g., Lee et al., 2022), so may be a physical consequence of the 3D simulation.

To investigate the dust-gas dynamics within the pressure bump and the potential for coagulation and dust clumping, we evaluate the level of turbulence of the gas and dust in the bump. The level of turbulence is quantified using the root mean squared dispersion velocity, $\sigma_{\mathrm{g,vel}}$ and $\sigma_{\mathrm{d,vel}}$, of the gas and dust particles within in the bump, respectively. We consider the bump to have a radial width of 2H (1H on either side of the peak) and we average over the full azimuthal and vertical range of the box. We find that $\sigma_{\mathrm{g,vel}} = 0.39$ and $\sigma_{\mathrm{d,vel}} = 0.18$, so then the turbulent viscosity parameter for gas is $\alpha = \sigma^2_{\mathrm{g,vel}}/c_s^2 = 0.15 \sim 10^{-1}$, and for dust $\alpha_d = 0.033 \sim 10^{-2}$ (with $c_s = 1$). These values are very high, $\sim 1 - 2$ orders of magnitude above the typical maximum quoted $\alpha \sim 10^{-3}$ for protoplanetary disks (e.g.,

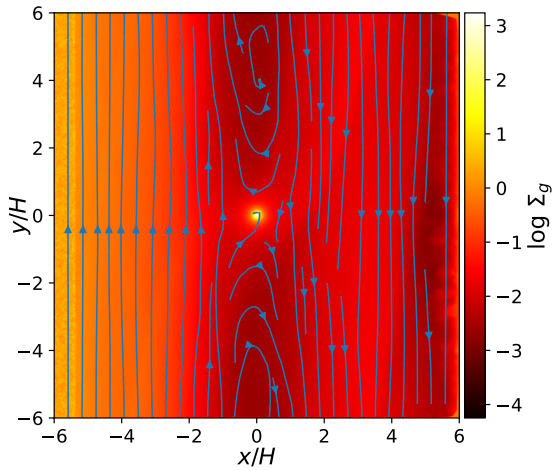

Figure 4.9: 2D snapshot of $\phi - r$ plane (slice at the planet location $z_p = 0H$), showing the gas density field with streamlines of the gas velocity field (blue lines) after $370\Omega^{-1}$. The planet is of mass $0.5M_{\rm th}$. We observe vortices at the center of the box due to shearing, since the gas velocity is in the reference frame of the center of the box. All our numerical experiments show the same qualitative behavior.

Flaherty et al., 2017), significantly increasing particle stirring and reducing dust settling at the midplane, which can also make dust coagulation and clumping more difficult. This level of turbulence in the gas may be due to perturbations by the planet, stirring up the gas which then interacts with the dust, making it turbulent. We then calculate the particle disk scale height using α and τ_S, finding $H_p = 0.78H$. We also evaluate the dust-to-gas mass ratio Z as a function of radius, shown in Figure 4.14. We calculate Z by dividing the box radially by smoothing length ($r_s = 0.1$) into sub-box elements with dimensions $L_{{\rm box},y} \times L_{{\rm box},z} \times r_s$. We add up the total gas mass and dust mass within each element and then take the dust to gas mass ratio. We find $Z_{\rm peak} = 0.84$ in the pressure bump. We repeat the same calculation, but

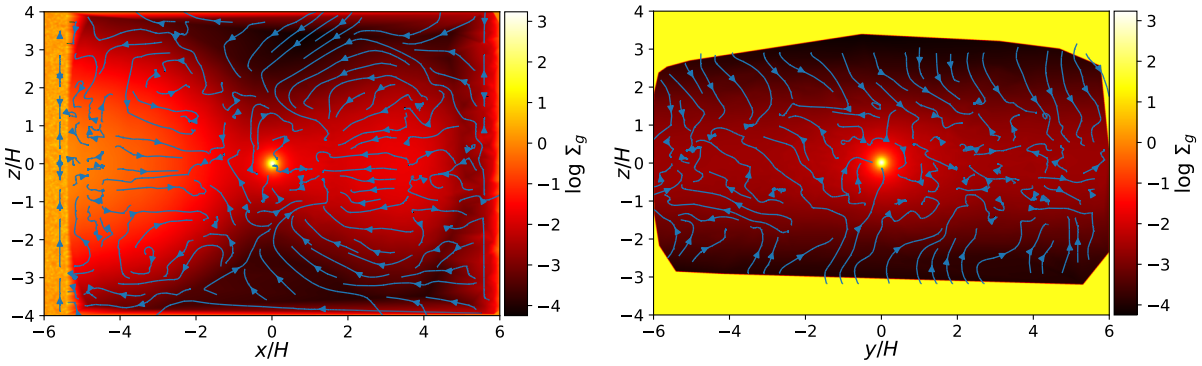

(a) **(b)**

Figure 4.10: 2D snapshot of a) $z - r$ plane and b) $z - \phi$ plane (slices taken at the planet location), showing the gas density field with streamlines of the gas velocity field (blue lines) after $370\Omega^{-1}$. The planet is of mass $0.5M_{\rm th}$.

reducing the vertical range of each box element to $H_{\rm p}$ (above and below the midplane), and find $Z_{\rm peak} = 1.50$ (also shown in Figure 4.14). We also note that we do not reach the steady state value $Z = 0.01$ to the right of the pressure bump. The parameters of the simulation are set such that the $Z = 0.01$ ratio is obtained when the disk is in its initial condition state, so we see a higher ratio due to the drop in gas density on the right of the planet as compared to its initial condition state, whereas the dust spawning rate does not change.

Finally, as a sanity check, we present the results for the simulation run with no planet. These results are shown in Figure 4.15 and will be discussed in Section 5.2.

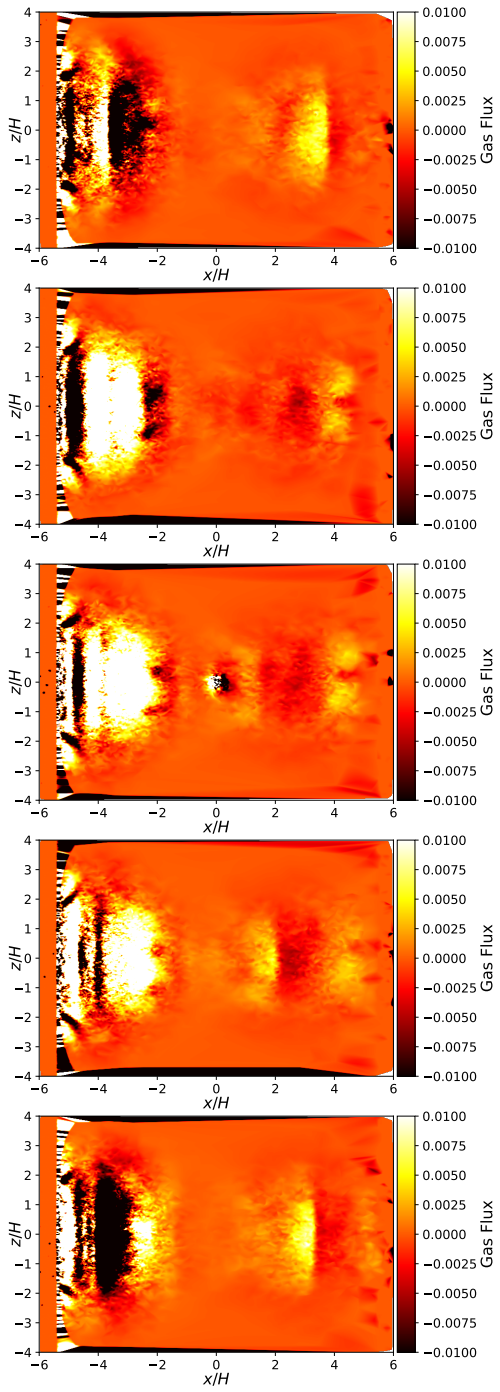

Figure 4.11: 2D snapshot of $z - r$ plane for a range of azimuthal locations, showing the radial component of the gas flux. The slices, from bottom to top, show azimuthal locations behind the planet at $y = -5H$ and $y = -1H$, at the planet location y_p (center panel), and then ahead of the planet at $y = 1H$ and $y = 5H$. We note a velocity direction change near the planet, where the gas flows radially towards it (accretion), compared to further away from the planet, where gas is being driven radially away by perturbations from the planet.

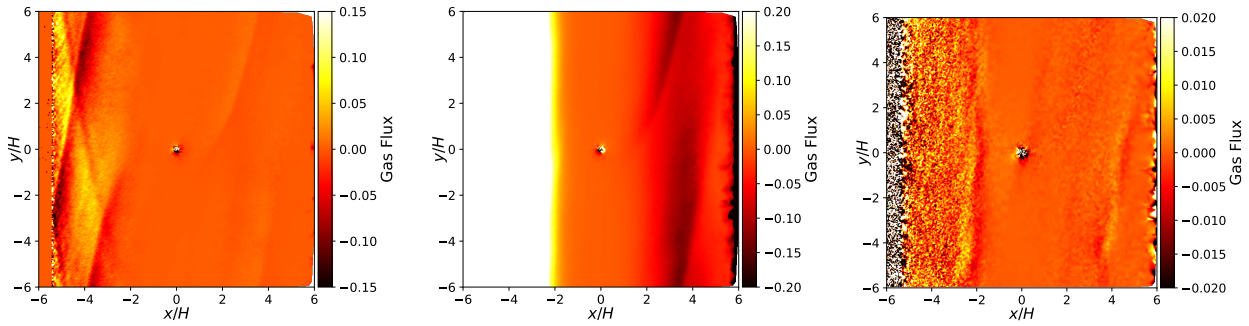

(a) Radial gas flux **(b)** Azimuthal gas flux **(c)** Vertical gas flux

Figure 4.12: 2D snapshot of $\phi - r$ plane at the planet location showing each of the directional components of the gas flux after $370\Omega^{-1}$.

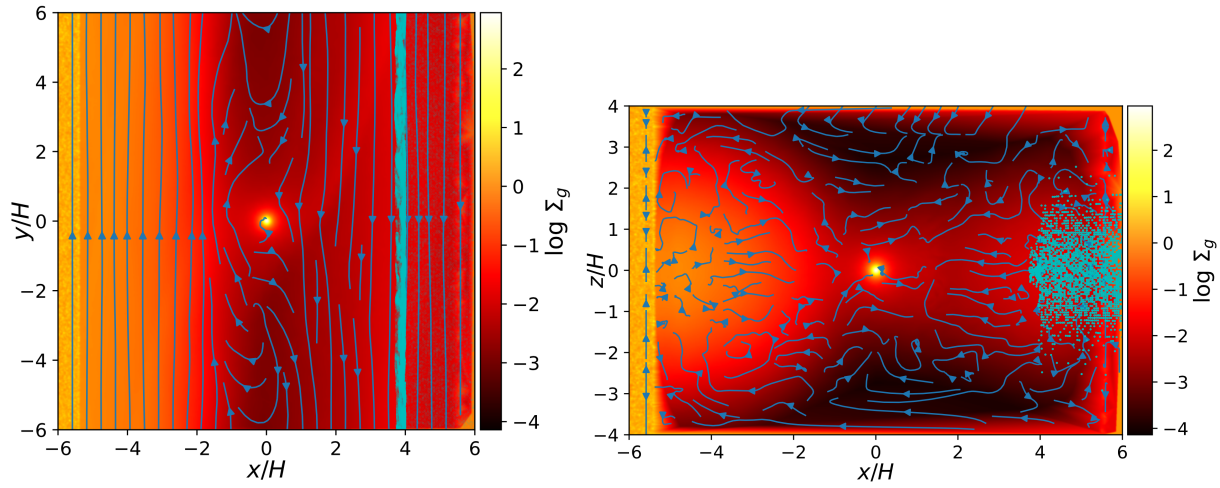

(a) **(b)**

Figure 4.13: 2D snapshot of a) $\phi - r$ plane and b) $z - r$ plane (slices taken at the planet location), showing the gas density field (background) and the spatial distribution of dust particles with $\tau_S = 0.1$ (cyan points), after $350\Omega^{-1}$. The pressure bump was created by a $0.5M_{\rm th}$ planet. We find that dust particles become trapped slightly outside the center of the bump, around $x \sim 4H$. Plot b) shows some dust settling, but turbulent mixing prevents total settling at the midplane and maintains dust suspension between $z \approx -2H$ to $2H$, with $H_{\rm p} = 0.78H$.

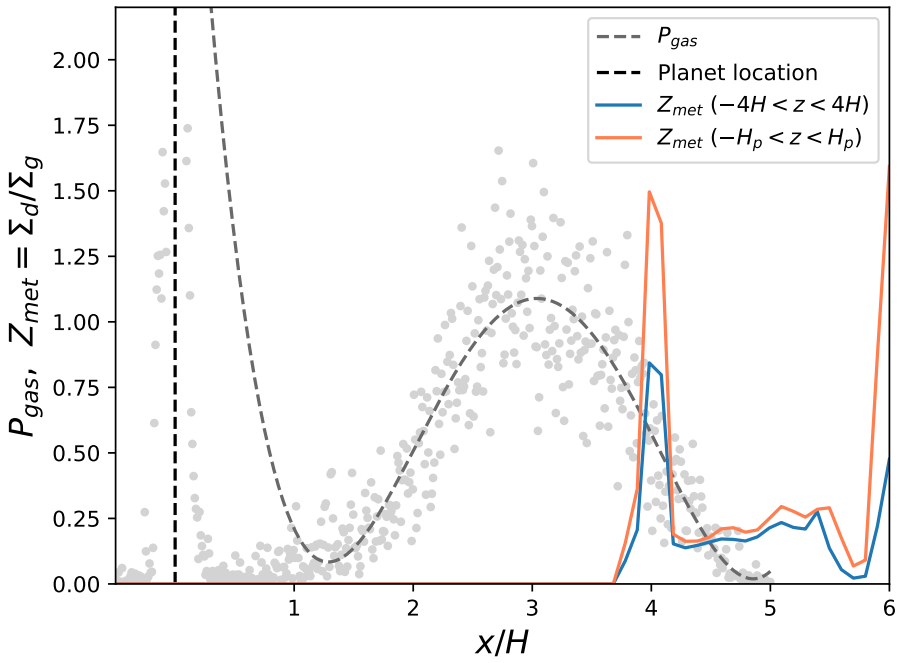

Figure 4.14: Azimuthally and vertically averaged dust-to-gas mass ratio profile (solid lines) and radial gas pressure profile (scatter points and dashed line) in the shearing box after $300\Omega^{-1}$. We observe the formation of a pressure bump near $x = 3H$, established by the $0.5M_{\rm th}$ planet located at $x = 0H$, and a peak in the dust-to-gas ratio Z_{met} around $x = 4H$, to the right of the pressure bump. The Z_{met} profiles are calculated using the same method, but differ by the vertical extent included in calculating the mass average. We find a value $Z_{\rm peak} = 0.84$ when the entire vertical extent of the box is considered (solid blue line), which is lower than $Z_{\rm peak} = 1.50$ when taking only $H_{\rm p} = 0.78H$ above and below the midplane (dashed purple line). This is expected as $H_{\rm p} < H$, so dust is more concentrated towards the midplane.

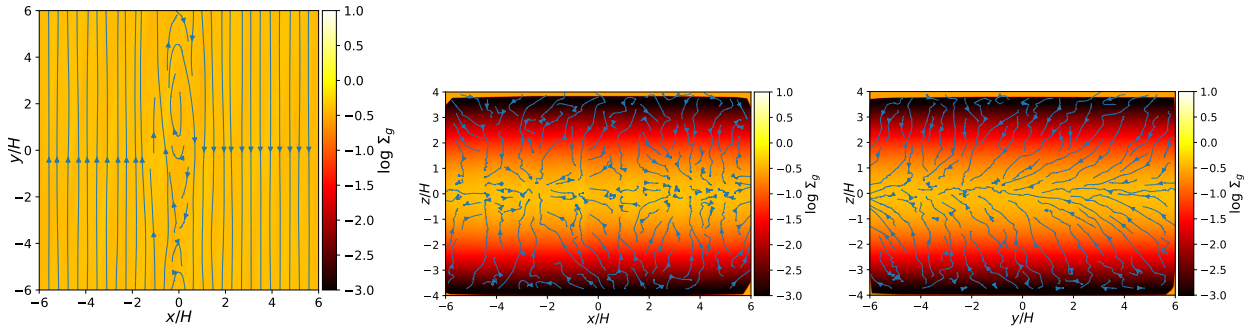

(a) **(b)** **(c)**

Figure 4.15: 2D snapshot of a) $\phi - r$, b) $z - r$, and c) $z - \phi$ planes (slices taken at the center of the shearing box), showing the gas density distribution and velocity streamlines for the case with no planet and no dust after $900\Omega^{-1}$.

Chapter 5

Discussion

5.1 2D Global Protoplanetary Disk

The 2D global disk simulation is still in the development stage. As such, this section will focus primarily on the next steps of the code development process. We have yet to establish a steady state disk setup (see Figure 4.8) as the boundaries continue to cause non-physical behaviour in the disk gas. Future work includes running follow up test cases in an attempt to further reduce the numerical error and numerical artifacts associated with the boundary conditions. We currently plan to implement three modifications in particular, but this is a constantly evolving process. The first will be to run further resolution tests, with the goal of testing the effects of increasing the resolution near the inner radius, as this area has the highest error and appears to be driving spurious density waves. We will also introduce a

damping term for the gas particles near the inner radius, which will damp the velocity back to its initial condition (according to Equation 3.8). Finally, we will investigate the effect of varying the width of the inner ghost particle ring, by filling more of the gap in the middle of the disk with ghost particles and by moving the boundary of the physical inner radius further out. Again, these future tests will be done with the aim of achieving the target precision ($\sqrt{\alpha} \sim 0.03$ see Section 4.1) for the disk gas properties (velocity, acceleration, and surface density).

Eventually, we will introduce a planet in the disk to establish the gas pressure bump and investigate the bump's dust trapping efficiency and the dust-gas dynamics within the bump. In order to effectively evaluate the physics from the code results, we must ensure that the behaviour is due to the underlying physics and not numerical errors. Spurious wave propagation may interfere with establishing a pressure bump, and consequently result in physically unreliable behaviour of the gas and dust, so we must first ensure that the numerical error causes perturbations on a scale smaller than the expected subsonic scale.

5.2 3D Local Shearing Box

We will begin our discussion of the 3D local shearing box results by considering the simplest test case, which is that with no planet, shown in Figure4.15. Without numerical error, the gas should be in steady-state as it is uniformly distributed in the azimuthal and radial directions, and is vertically stratified such that the gas is in hydrostatic equilibrium (vertical

pressure gradient force balanced with gravitational force). Figure 4.15a and 4.15c appear to behave as expected, whereas in Figure 4.15b, there appears to be a net gas flow in the vertical direction, suggesting that the disk may be in a transient state due to numerical effects, so the code is trying to re-establish an equilibrium solution. We note, however, that when comparing consecutive snapshots, there appears to be a cyclical behaviour as the direction of the net vertical flow of the gas inverts approximately once every orbital period. This behaviour may be due to insufficient resolution in the vertical direction, in particular because the resolution diminishes in the outer layers ($\sim$ the outer 2H) where the gas density is much lower than at the midplane.

It is necessary to investigate this effect further because the impact on the gas dynamics during the transient state may cause non-physical behaviour if the planet is introduced before a steady state is reached. The perturbations from the planet may amplify the transient state, and their interaction could interfere with the waves being driven by the planet, consequently affecting the pressure bump that is to be established by these waves. So, if it is the case that the code requires a higher resolution as well as time to establish a steady-state, we must allow this state to be reached before introducing the planet to ensure that the results are physically accurate and not due to numerical artifacts.

We also consider whether we expect to see dust clumping by the SI (see Section 2.4.1) within the pressure bump using the dust-to-gas mass ratio from our simulation results. Applying Equation 2.8 for $\tau_S > 0.015$, we find $\epsilon_{\text{crit}}(\tau_S = 0.1) = 1.54$. Then applying

Equation 2.9, with $\Pi = 0.05$ and $\alpha = 0.15$, we find $Z_{\rm crit} = 1.20$. From Figure 4.14, we find $Z_{\rm peak} = 0.84 < Z_{\rm crit}$ in the pressure bump for the full vertical extent of the box, whereas $Z_{\rm peak} = 1.50 > Z_{\rm crit}$ when calculated within only $H_{\rm p}$ above and below the midplane. We therefore expect to see dust clumping by the SI within the particle disk scale height, but not necessarily throughout the entire vertical range of the disk. As part of the next steps, we hope to directly simulate dust clumping and potentially pebble accretion. We would also like to turn on particle self-gravity to further investigate dust clumping in the pressure bump, according to the conditions outlined in Section 2.4.2.

Chapter 6

Conclusion

In this thesis, we investigate dust trapping in protoplanetary disks by gas pressure perturbations established by an embedded planet, and report on their ability to coagulate and clump dust particles. To do so, we modify the GIZMO code so that it is appropriate for the domain and timescales of our simulations and develop the initial condition setups and boundary conditions of the disk for both global and local, to reduce numerical error and achieve a specified target precision in the results. Our 3D simulation uses $M_p = 0.5 M_{\rm th}$ to establish the pressure bump and dust grains with $\tau_S = 0.1$, and from our preliminary analysis, we find that within the pressure bump and vertical particle disk scale height, the dust-to-gas mass ratio exceeds the critical value required to trigger clumping by the streaming instability. We then expect to see clumping. The target precision for our 2D global simulation has still not been achieved, likely due to numerical artifacts caused by

the boundaries, such as spurious wave propagation. Further code development is required to reduce the numerical error, including introducing velocity damping at the boundaries and increasing particle resolution. The next steps will then be to introduce a planet and dust to investigate the effect of the global setting on the dust-gas dynamics in the disk and within the pressure bump.

Bibliography

Andrews, S. M., Huang, J., Pérez, L. M., et al. 2018, The Astrophysical Journal Letters, 869, L41

Bai, X.-N., & Stone, J. M. 2010, The Astrophysical Journal Letters, 722, L220

Bertoldi, F., & McKee, C. F. 1992, Astrophysical Journal, Part 1 (ISSN 0004-637X), vol. 395, no. 1, p. 140-157., 395, 140

Carrera, D., & Simon, J. B. 2022, The Astrophysical Journal Letters, 933, L10

Carrera, D., Simon, J. B., Li, R., Kretke, K. A., & Klahr, H. 2021, The Astronomical Journal, 161, 96

Chiang, E., & Goldreich, P. 1997, The Astrophysical Journal, 490, 368

D'Alessio, P., Cantö, J., Calvet, N., & Lizano, S. 1998, The Astrophysical Journal, 500, 411

Dong, R., Li, S., Chiang, E., & Li, H. 2017, The Astrophysical Journal, 843, 127

D'Alessio, P., Calvet, N., & Hartmann, L. 2001, The Astrophysical Journal, 553, 321

Flaherty, K. M., Hughes, A. M., Rose, S. C., et al. 2017, The Astrophysical Journal, 843, 150

Fromang, S., Lyra, W., & Masset, F. 2011, Astronomy & Astrophysics, 534, A107

Fung, J., Artymowicz, P., & Wu, Y. 2015, The Astrophysical Journal, 811, 101

Fung, J., & Ono, T. 2021, The Astrophysical Journal, 922, 13

Gerbig, K., Murray-Clay, R. A., Klahr, H., & Baehr, H. 2020, The Astrophysical Journal, 895, 91

Goodman, J., & Rafikov, R. 2001, The Astrophysical Journal, 552, 793

Hopkins, P. F. 2015, Monthly Notices of the Royal Astronomical Society, 450, 53

—. 2016, Monthly Notices of the Royal Astronomical Society, 462, 576

—. 2017, Monthly Notices of the Royal Astronomical Society, 466, 3387

Hopkins, P. F., & Raives, M. J. 2016, Monthly Notices of the Royal Astronomical Society, 455, 51

Klahr, H., Pfeil, T., & Schreiber, A. 2018, arXiv preprint arXiv:1806.03896

Lee, E. J. 2024, The Astrophysical Journal Letters, 970, L15

Lee, E. J., Fuentes, J., & Hopkins, P. F. 2022, The Astrophysical Journal, 937, 95

Li, R., & Youdin, A. N. 2021, The Astrophysical Journal, 919, 107

Lin, D., & Papaloizou, J. 1993, in Protostars and planets III, 749–835

Liu, M., & Liu, G. 2010, Archives of computational methods in engineering, 17, 25

Mamajek, E. E. 2009in , American Institute of Physics, 3–10

Monaghan, J. J. 1992, In: Annual review of astronomy and astrophysics. Vol. 30 (A93-25826 09-90), p. 543-574., 30, 543

—. 2005, Reports on progress in physics, 68, 1703

Moseley, E. R., Squire, J., & Hopkins, P. F. 2019, Monthly Notices of the Royal Astronomical Society, 489, 325

NASA Exoplanet Archive. 2024, Planetary Systems, Version: 2024-08-04 17:10, NExScI-Caltech/IPAC, doi: 10.26133/NEA12

Pinilla, P., Birnstiel, T., Ricci, L., et al. 2012, Astronomy & Astrophysics, 538, A114

Sekiya, M., & Onishi, I. K. 2018, The Astrophysical Journal, 860, 140

Seligman, D., Hopkins, P. F., & Squire, J. 2019, Monthly Notices of the Royal Astronomical Society, 485, 3991

Shakura, N. I., & Sunyaev, R. A. 1973, Astronomy and Astrophysics, Vol. 24, p. 337-355, 24, 337

Su, K.-Y., Hopkins, P. F., Hayward, C. C., et al. 2017, Monthly Notices of the Royal Astronomical Society, 471, 144

Testi, L., Natta, A., Shepherd, D., & Wilner, D. 2003, Astronomy & Astrophysics, 403, 323

Weidenschilling, S. 1977, Monthly Notices of the Royal Astronomical Society, 180, 57

Youdin, A. N., & Goodman, J. 2005, The Astrophysical Journal, 620, 459

Youdin, A. N., & Lithwick, Y. 2007, icarus, 192, 588

Zhang, K., Bergin, E. A., Blake, G. A., Cleeves, L. I., & Schwarz, K. R. 2017, Nature Astronomy, 1, 0130

Zhang, K., Booth, A. S., Law, C. J., et al. 2021, The Astrophysical Journal Supplement Series, 257, 5